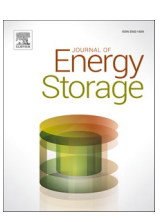
ELSEVIER

Contents lists available at ScienceDirect

Journal of Energy Storage

journal homepage: www.elsevier.com/locate/est



Research Papers

Optimal thermal management of electric vehicle battery systems using serpentine minichannel cold plates with intersecting V-shaped minichannels

Ahmed Mahmood ^{a,b,*}, Gregory de Boer ^a, Timothy Cockerill ^a, Muhammad F.B. Raihan ^a, Harvey Thompson ^a, Jochen Voss ^c

- ^a School of Mechanical Engineering, University of Leeds, Leeds, LS2 9JT, UK
- ^b Technical Engineering College of Mosul, Northern Technical University (NTU), Mosul, 41001, Iraq
- ^c School of Mathematics, University of Leeds, Leeds, LS2 9JT, UK

ARTICLE INFO

Keywords: Li-ion batteries Electric vehicles Thermal management Computational fluid dynamics Machine learning Multi-objective design optimization comsol multiphysics®

ABSTRACT

Environmental concerns are promoting the shift towards electric vehicles (EVs) from internal combustion-based vehicles. Lithium ion (Li-ion) batteries are currently the dominant power source option for modern electric vehicles (EVs); however, their operating temperatures need to remain within an allowable safety range in order to preserve battery lifetime and avoid thermal runaway. Accordingly, high-performance battery thermal management systems (BTMSs) are needed for safe and efficient battery operation. These challenges are addressed here using a novel machine learning (ML)-enabled multi-objective optimization (MOO) approach for BTMS based on serpentine minichannel cold plates with intersecting V-shaped minichannels (SMCCP-IVSMC). The SMCCP-IVSMC configuration is optimised here for the first time, subject to four competing objectives, namely the battery maximum temperature (T_{max}), water pumping power (P_w), battery temperature standard deviation (T_σ), and the mass of the cold plate (MCP). Reducing MCP has not been considered previously; however, it plays a vital role in improving both the energy consumption and manufacturing costs of cooling systems. A thermal model based on empirical heat generation with a conjugate heat transfer model in the cold plates is developed and validated comprehensively. Surrogate modeling based on both Radial Basis Functions (RBFs) and Gaussian Process Regression (GPR) shows the latter is the most effective. This is used to explore the trade-offs between the competing objectives (T_{max} , P_w , T_σ , and M_{CP}). A novel hybrid optimization approach is developed, integrating GPR, Generalized Differential Evaluation (GDE3) and Technique for Order Preference by Similarity to an Ideal Solution (TOPSIS) methods to determine the best compromise solutions (BCSs) among the set of Pareto optimal solutions. The optimisation results identify numerous options for improving performance significantly, beyond the current benchmark design. In addition to reductions in the maximum temperature, operating costs can be minimised by reducing water pumping power by over 68.7 %, and manufacturing costs minimised by reducing the mass of the cold plate heat exchangers by over 22.8 %. The top-ranked BCS using equally weighted TOPSIS has also been identified, which enables all four objectives to be reduced simultaneously.

1. Introduction

Combustion engine-powered vehicles are one of the most important contributors to greenhouse gas emissions (GHGs) [1]. They use only about 20 % of fuel energy for vehicle movement, whereas EVs transform 85 %–90 % of their stored energy into vehicle kinetic energy [2]. Accordingly, vehicle manufacturing is shifting towards more

sustainable, quieter, and environmentally friendly alternatives. It is generally agreed that using electric vehicles (EVs) is essential for achieving the net-zero emission goals [3].

Li-ion batteries are broadly used in EVs due to their longevity, low self-discharge rate, and high power density [4]. However, they can suffer from important practical limitations, one of which is a rapid rise in temperature beyond the acceptable operating range that reduces the

^{*} Corresponding author at: School of Mechanical Engineering, University of Leeds, Leeds, LS2 9JT, UK.

E-mail addresses: mnamma@leeds.ac.uk (A. Mahmood), g.n.deboer@leeds.ac.uk (G. de Boer), t.cockerill@leeds.ac.uk (T. Cockerill), m.raihan@leeds.ac.uk (M.F.B. Raihan), h.m.thompson@leeds.ac.uk (H. Thompson), j.voss@leeds.ac.uk (J. Voss).

battery performance, shortens its useful lifetime, and can lead to localised deterioration in the battery pack [5]. Another is the uneven temperature distribution that can cause a short circuit in the battery [6]. Prolonged operating temperatures of 50 °C or above accelerate its aging and eventually lead to a decline in its usable capacity [7]. To ensure continuous optimal performance, the optimal working temperature range should be 20 °C to 40 °C [8], and the temperature differences from module to module and cell to cell should generally be within 5 °C [6]. Accordingly, effective battery thermal management systems (BTMSs) are necessary to ensure the battery modules operate safely and effectively.

There is a wide range of thermal management technologies applied to a diverse range of applications, such as in buildings [9,10], electronics [11], data centres [12,13], EVs [14-16], fuel cells [17,18], solar panels [19–21], aerospace [22], etc. These include liquid cooling [23–26], air cooling [27-29], heat pipe cooling [30,31], phase change materials (PCMs) [32-35], and a variety of hybrid cooling systems [36-39]. Aircooled systems are simple and cheap, but they have low thermal efficiency, making them unsuitable for long-distance or high-powered EVs [40]. Passive cooling systems like PCMs and heat pipes can be used to regulate the battery's temperature using latent heat and offer several advantages, such as good temperature uniformity, low operating costs, and no extra power consumption [41]. However, they are less effective at temperature regulation [40]. PCMs' thermal conductivities are limited, and heat transfer deteriorates after they have completely melted [42]. The volume of these materials changes throughout the resolidification process after melting and becomes difficult to manage [43]. The main issue with heat pipe cooling systems is their safety; a short circuit can occur due to fluid leakage on the battery cells, causing vehicle failure and possibly death [44]. Furthermore, these systems need secondary heat exchangers to cool their condensers, necessitating further research before they can successfully cool electric vehicle batteries. Hybrid systems combine the advantages of the individual cooling systems mentioned above by integrating more than one of these systems to overcome their limitations. However, these also have drawbacks due to their increased weight, large volume, and high energy consumption [45]. Among these cooling systems, liquid cooling can be very effective due to its large thermal conductivity and specific heat capacity, and more compact structure [46]. Its heat dissipation performance is roughly three times better than air-cooled battery modules [47]. Accordingly, Liquid cooling, using water or coolant, is currently the predominant cooling method used by automotive manufacturers to manage battery packs effectively and has therefore become an important research topic [48-50].

Liquid-cooled BTMS generally rely on two different mechanisms: direct contact (immersive) or indirect contact of liquid with the battery cells [51]. Direct contact liquid cooling is highly effective at transferring heat from battery cells to the coolant and can also be less expensive and simpler than indirect contact cooling [52]. However, indirect contact liquid BTMS is more widely used in commercial EVs, including the Tesla Model 3, BYD e5 450, Dihao EV 450, and Chevrolet Volt [53] due to concerns related to safety and the risk of coolant leakage [52,54]. Indirect contact liquid BTMSs have many configurations, such as tubes, jackets, and cold plates, with various mini-channel designs that transfer the cooling fluid. Cold plates have recently become the most popular configuration due to their advantages in terms of low risk of leakage, easy maintenance, seasonal cooling and heating abilities, and scalability for larger surfaces [55].

The performance of cold plates depends critically on the configuration and arrangement of their mini-channel design. Several cold plate channel configurations have been investigated recently, including those with straight [23,56], U-bend [57,58], serpentine [59,60], pumpkin [61], bionic fishbone [62], honeycomb [63], and butterfly [64] channels. Serpentine channel designs have received the most attention due to their wide-ranging practical applications [59] and their ability to periodically disrupt and redevelop thermal and hydraulic boundary layers,

improving heat transfer significantly [65]. Monika and Datta [66] conducted a comparative study of six different types of cold plate designs with identical channel volumes: serpentine, straight, U-bend, spiral, pumpkin-shaped, and hexagonal structural channels. Their results indicate that although the pumpkin model has a smaller pressure drop, the serpentine and hexagonal shapes significantly enhance temperature uniformity. Wang et al. [67] evaluated the thermal performance of a liquid cooling BTMS with serpentine micro-channels and found that the best design to lower the maximum and average temperatures of the battery module was to alternately arrange the water inlets and outlets on one side of the cooling plates. A variable cross-section double serpentine-channel cold plate (VCDSCP) was recently proposed by Pu et al. [59]. The results indicate that at higher discharge rates, the VCDSCP design lowers the maximum temperature by 0.54 K and the maximum temperature difference by 0.62 K compared to the conventional serpentine-channel cold plate. The results also showed that the VCDSCP design resulted in a maximum pressure drop (Δp) decrease of 80.8 % and an increase of 25.5 % in the performance evaluation criterion (PEC) at a coolant flow rate of 0.2 g/s.

The thermal and hydraulic performances of minichannels in thermal management applications have been enhanced using many devices that increase turbulence, introduce secondary flows, increase fluid mixing, and disrupt the thermal and hydraulic boundary layers, including gyroids, cavities, ribs, and vortex generators. Saghir and Yahya [68] proposed a solid gyroid structure within the cold plate and discovered that besides creating a more uniform temperature distribution, the Nusselt number increased by 85 % compared to the conventional channel configuration. Kaewchoothong et al. [69] indicated that the heat transfer performance of the wavy-winglet rib design increased heat transfer between 10 %-32 % depending on rib designs, albeit with a larger pressure drop. Zhu et al. [50] examined a unique liquid-cooled plate with a discrete, inclined, and alternating arrangement of ribs and grooves to enhance thermal performance. Compared to a conventional straight-channel design, the innovative cold plate obtained a 0.74 °C lower maximum battery temperature and a 0.18 °C lower temperature standard deviation, with a pressure drop of 55.37 Pa higher than the conventional one. Sakkera et al. [70] assessed innovative designs of serpentine channel heat sinks that have rectangular ribs with both rectangular (RRRG) and triangular grooves (RRTG), and they found that the average Nusselt number increase for RRRG and RRTG is 46 % and 36 %, respectively, compared to a traditional smooth channel heat sink. Nevertheless, RRRG and RRTG have average pressure drops that are 56 % and 35 % higher, respectively, than those of smooth channel heat sinks. Xu et al. [71] investigated the effects of adding three distinct vortex generators - triangle, trapezoid, and semicircle - to the liquid cooling straight mini-channel of cold plates on the battery's heat dissipation capacity and temperature uniformity. They found that, while providing the same heat dissipation efficiency, the semi-circular vortex generators had a lower pressure drop than the trapezoidal and triangular vortex generators, by 15.9 % and 20.5 %, respectively.

A number of studies studied how cold plate performance can be enhanced by using the secondary flow minichannels between the main minichannels. Several heat sink studies in the literature demonstrate that secondary flows in the serpentine microchannel can enhance heat transfer without increasing the pressure drop because they increase the surface area for heat transfer and allow the cooling fluid to pass through them at a lower fluid velocity, see e.g. [72,73]. Far fewer studies have considered using a serpentine configuration with the secondary flow paths in the MCCP of the BTMS. Recently, Fan et al. [74] enhanced the design of a liquid cooled plate with a conventional serpentine channel by incorporating elliptical grooves and unidirectional secondary channels. Their simulation results show that, even though the enhanced design has slightly lower thermal performances, including the maximum temperature and average maximum temperature difference of the battery modules, compared to the original serpentine cold plate, it has significantly reduced the pumping power requirement, and improved the

cooling efficiency coefficient, which is the ratio of heat dissipation capacity to power consumption. Furthermore, two numerical studies enhanced the performance of the liquid-based thermal management system for prismatic lithium-ion batteries by integrating V-shaped intersecting minichannels into traditional serpentine channels [75,76]. On the basis of their brief parameter studies this particular MCCP configuration was found to show very promising thermo-hydraulic performance, but that systematic optimization would be needed to minimise the effect of the additional mass on EV performance. Previous studies have shown that a 10 % reduction in the vehicle's mass can result in a 5.5 %-8 % reduction in energy consumption [77]. Reducing the vehicle's weight also leads to better acceleration performance and reduced braking distances [78]. Accordingly, recent studies have concentrated on and will continue to focus on lightweight BTMSs. For instance, Dileep et al. [79] proposed lightweight T-shaped cold plate designs that account for only 20.7 % of the overall module weight. Zhou et al. [80] proposed three hybrid BTMS designs with different geometries, using phase change materials and honeycomb-shaped cold plates for the liquid cooling of twelve cylindrical Li-ion batteries. They found that one of these designs could decrease the BTMS weight from 0.35 kg to 0.19 kg. Khoshvaght-Aliabadi et al. [81] also proposed three BTMS designs for cooling cylindrical lithium-ion cells, which include designs with 1, 3 and 5 cooling units. Their results indicated that while both the BTMS with three and five cooling units provided closer values of maximum temperature difference across the battery module-5.4 K and 4.1 K, respectively, compared to the BTMS with one cooling unit at 22.5 K, the BTMS with three cooling units resulted in approximately a 12 % reduction in the weight index (the weight ratio of the BTMS to the battery module) compared to the system with five cooling units. Accordingly, this paper is novel in two key aspects. It is the first to develop and apply a novel ML-enabled multi-objective optimization (MOO) approach for the thermal management of SMCCP-IVSMC cold plate configurations based on TOPSIS approaches and is the first to attempt to reduce the cold plate mass in addition to the other thermohydraulic performance indicators, including the maximum temperature, water pumping power and temperature variation over the cold plate.

The paper is structured as follows: Section 2 describes the numerical methodology used for the battery thermal management prototype, and provides an in-depth description of the physical problem, the conjugate heat transfer model, and its associated governing equations and boundary conditions. Section 3 focuses on the validation and verification of the proposed numerical model and presents grid- and time-stepsensitivity studies. A comprehensive sensitivity analysis of the input design variables and their effects on the output objective parameters is presented in Section 4, and the optimization methodologies are described in Section 5, including the sampling method, surrogate models, optimization algorithm, and TOPSIS approaches. Section 6 presents a comprehensive analysis of the simulation and optimization results. Finally, conclusions are drawn in Section 7.

2. Numerical methodology

2.1. Physical problem

The BTMS developed by Liu et al. [75], is analysed. It is composed of several 8.0 Ah prismatic LiFePO $_4$ Li-ion battery cells, each with a size of 124 mm \times 79 mm \times 17 mm, and serpentine minichannel cold plates with intersecting V-shaped minichannels (SMCCP-IVSMC) incorporated between consecutive battery cells. The cell specifications are given in Table 1 [82]. The anode and cathode materials for the cell are graphite and lithium iron phosphate (LiFePO $_4$), respectively; the electrolyte consists of ethylene carbonate, dimethyl carbonate, and ethyl methyl carbonate (EC/DMC/EMC); and the inner core of the battery is wrapped by the Al alloy casing.

The SMCCP-IVSMC aims to mitigate the hotspots and ensure greater

Table 1
Specifications of LiFePO₄ battery cell.

Contents	Battery cell
Active area dimensions (mm)	17 × 79 × 124
Mass (g)	328
Rated capacity (Ah)	8.0
Normal voltage (V)	3.20
Specific heat (J/kg·K)	1305
Thermal conductivity (W/m.K)	2.6

temperature uniformity. Initial studies have shown that the SMCCP-IVSMC design can result in a substantially lower pressure drop compared to the standard SMCCP because the secondary flow minichannels result in slower flow than the standard SMCCP. The BTMS is shown in Fig. 1; Fig. 1a displays the BTMS layout, and Fig. 1b shows the configuration, boundary conditions and geometrical parameters for half of the domain of a single battery cell and a SMCCP-IVSMC, where symmetry has been exploited. During the discharging process of Li-ion battery cells, Li-ions migrate through the electrolyte from the anode (negative electrode) to the cathode (positive electrode). At the same time, electrons move simultaneously via the external circuit to generate electricity. This process involves several chemical and physical phenomena, including the diffusion of Li-ions (insertion and de-insertion) within solid electrode particles, the diffusion of Li-ions in the electrolytes and the electrochemical reactions that occur at the solid-liquid electrolyte interface, which generate a substantial amount of heat. The performance of the BTMS is simulated for the worst-case scenario, where all battery cells are fully discharged at a rapid C-rate (9C).

2.2. Numerical modeling

A three-dimensional conjugate heat transfer (CHT) model is used to simulate the interaction between conductive heat transfer in the solid domains and convection in the fluid. Finite element analysis (FEA) is employed as a numerical approach inside COMSOL Multiphysics® (v.6.0) to solve the governing equations subject to the boundary conditions. The continuity and momentum equations of the cooling fluid (water) within the mini channels are given, respectively, by the following:

$$\frac{\partial \rho_{w}}{\partial t} + \nabla \bullet (\rho_{w} \bullet U_{w}) = 0 \tag{1}$$

$$\frac{\partial(\rho_{w} U_{w})}{\partial t} + \nabla \bullet (\rho_{w} \bullet U_{w} U_{w}) = -\nabla p_{w} + \mu_{w} \nabla^{2} U_{w}$$
 (2)

where ρ_w , μ_w and p_w are the cooling water's dynamic density, viscosity, and pressure, respectively. U_w is the water velocity vector with the components u, v, and w in the x-, y-, and z- directions, respectively. ∇ is the gradient operator and is defined as follows:

$$\nabla = \frac{\partial}{\partial x} \mathbf{i} + \frac{\partial}{\partial y} \mathbf{j} + \frac{\partial}{\partial z} \mathbf{k}$$
 (3)

The energy conservation equations for the water and cold plate are given, respectively, by the following:

$$\frac{\partial \left(\rho_{w} \bullet C_{p_{w}} \bullet T_{w}\right)}{\partial t} + \nabla \bullet \left(\rho_{w} C_{p_{w}} U_{w} T_{w}\right) = \nabla \bullet \left(K_{w} \nabla T_{w}\right) \left(4\right) \tag{4}$$

$$\frac{\partial \left(\rho_{CP} \bullet C_{PCP} \bullet T_{CP}\right)}{\partial t} = \nabla \bullet (K_{CP} \nabla T_{CP}) \tag{5}$$

where C_{p_W} , K_w , and T_w are the specific heat capacity, thermal conductivity, and the temperature of the cooling water, respectively. ρ_{CP} , K_{CP} , C_{PCP} and T_{CP} are the dynamic density, thermal conductivity, specific heat capacity, and the temperature of the cold plate, respectively.

The energy conservation equation for each Li-ion battery cell is as

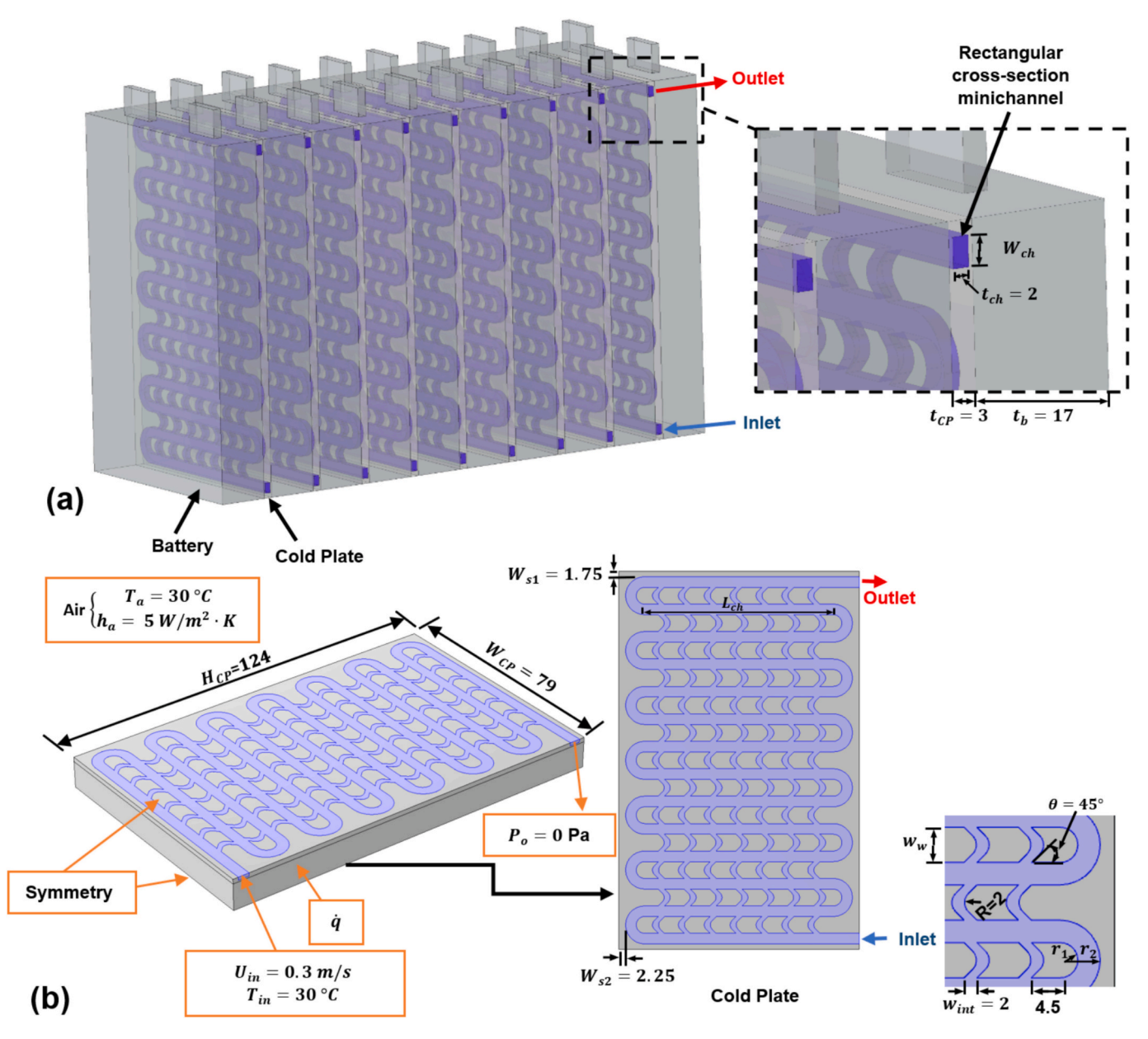


Fig. 1. Schematics of the BTMS based on SMCCP-IVSMC: (a) battery module; (b) half of the domain of a single battery unit and a SMCCP-IVSMC (units: mm).

follows

$$\rho_b C_{p_b} \frac{\partial T}{\partial t} = \nabla \bullet (K_b \nabla T) + \dot{q}$$
 (6)

where $\rho_b,\, C_{P_b},\,$ and K_b are the dynamic density, specific heat capacity, and thermal conductivity of the battery cell, respectively. \dot{q} is the heat generation rate of each battery cell. The heat generation rates within Liion batteries need to be determined accurately to provide high-fidelity heat transfer models of Li-ion-based BTMSs. Numerous earlier studies have used the major simplifying, yet physically unrealistic, assumption that the heat generation rate is steady [83]. The use of time-dependent models of the heat generation rate is much more realistic. These can be determined using theoretical modeling, such as the Newman pseudotwo-dimensional (P2D) model [84], the Newman, Tiedemann, Gu, and Kim (NTGK) model [85,86], and the equivalent circuit model (ECM) [87–89]. The P2D model is frequently employed for physics-based electrochemical-thermal modeling, considering the mobility of lithium ions through the solid electrode particles as well as the reaction kinetics at the electrode-electrolyte interfaces [90]. However, this model is both

complex and computationally expensive and depends on a large number of often uncertain parameters [23]. The NTGK, a semi-empirical model developed by Kwon et al. [86], is set up by curve fitting the experimental data and has been proved by several studies to be effective for predicting the fast heat evolution of Li-ion batteries [91]. From the thermal management perspective in high-performance EVs, the ECM can accurately represent the non-linear thermo-electrical behaviour of Li-ion batteries [92]. ECMs have provided an effective balance between complexity and precision, and their physical variables are not only readily interpretable but also comprehensible [90]. This study uses a time-dependent heat generation rate that was previously established by Sheng et al. [82] using the ECM based on two main experiment methods, i.e., the hybrid pulse power characterization (HPPC) method and the potentiometric method. This heat generation rate expression has been used successfully in a number of BTMS studies to simulate the heat generation that occurs within Li-ion process batteries during the discharge [23,75,76,82,93–97]. Accordingly, the following time-dependent heat generation rate expression from Sheng et al. [82], is employed at 9C:

$$\dot{q} = 319.6 - 2719.0 SOC + 15148.5 SOC^2 - 43018.3 SOC^3 + 63645.5 SOC^4 - 46817.9 SOC^5 + 13527.5 SOC^6$$
 (7)

where the heat generation rate is estimated from the above equation in (kW/m^3) and SOC, the cell state of charge, is given by:

$$SOC = 1 - I \bullet t/C \tag{8}$$

where I and C are the discharge current and nominal capacity of the battery cell, respectively, and t is the discharge time.

The thermo-physical properties of the materials used in the BTMS simulation are summarized in Table 2 [75].

The generalized- α numerical approach is used as the time-stepping method for the time-dependent solver when solving the CHT model for BTMS-based SMCCP-IVSMC design with a (2 s) time step. The relevant boundary conditions and assumptions that are used in the numerical solutions are listed in Table 3.

The performance of the BTMS is evaluated using the battery's maximum temperature (T_{max}), temperature standard deviation of the battery cells (T_{σ}) , the water pumping power (P_{w}) , and the mass of the material for each cold plate (M_{CP}). These are selected for the following reasons: (i) reducing the battery's maximum temperature is essential to constrain it within the allowable operating temperatures, which would otherwise accelerate the aging process, shorten battery lifetime, or even cause thermal runaway [98]. (ii) Reducing the temperature standard deviation ensures a more uniform temperature distribution, which reduces the risk of aging of the local electrode materials around thermal hotspots and accelerated battery failure [99,100]. (iii) Reducing the pumping power increases the driving range of EVs. (iv) The weight of the battery pack also has a significant impact on both driving range and EV efficiency (a lighter battery pack consumes less energy, leading to a longer driving range) [101]. Although liquid cooled BTMS provide effective cooling, they are considered a heavyweight thermal management option [43,102]. Accordingly, the present research also considers minimizing the mass of the cold plate material to reduce both the energy consumption and material cost. The above four performance metrics are given, respectively, by:

$$T_{max} = \text{Max}(T) \tag{9}$$

$$T_{\sigma} = \sqrt{\frac{\int_{A} (T - T_{\alpha \nu})^{2} dA}{\int_{A} dA}}$$
 (10)

$$P_{w} = \Delta p \times \dot{Q} \tag{11}$$

$$M_{CP} = \rho_{CP} \bullet V_{CP} \tag{12}$$

where the A is the battery cells area. T_{av} represents the average temperature of the battery cells, and is given by:

$$T_{av} = \frac{\int_A T \, dA}{\int_A \, dA} \tag{13}$$

 Δp is the pressure drop of the water in the mini channels (Pa). \dot{Q} is the volumetric flow rate in (m^3/s) , $(\dot{Q}=A_{ch}\times U_{in})$, and A_{ch} is the cross-sectional area at the inlet of the minichannel (m^2) . V_{CP} is the volume of

Thermo-physical properties of the materials used in BTMS simulation of SMCCP-IVSMC design.

Materials	Density (ρ) kg/m^3	Thermal conductivity (K) W/m·K	Heat capacity (C_p) $J/kg\cdot K$	Dynamic viscosity (μ) Pa .s
Cooling water	998	0.6	4200	0.001003
Cold plate	2719	202.4	871	_
Battery	1969.6	2.6	1305	_

Table 3The boundary conditions for BTMS based on SMCCP-IVSMC design.

Locations	Fluid conditions	Thermal conditions
Inlet	Laminar flow Inlet flow velocity (U _{in} = 0.3 m/s)	$Temperature \; (T) = T_{in} = 30^{\circ} C$
Outlet	The pressure outlet	In the normal direction, the
	boundary condition.	temperature gradient is zero.
	$p=p_o=0$	Outflow -n.q = 0
Interface surface	No–slip condition. $U_w = 0$	$-K_{CP} \left. \frac{\partial T_{CP}}{\partial n} \right _{\Gamma} = -K_{w} \frac{\partial T_{w}}{\partial n} \right _{\Gamma}$
		$T_{CP,\Gamma} = T_{w,\Gamma}$
Incompressible flow	$rac{\partial ho_w}{\partial t} + ho_w abla ullet oldsymbol{U_w} = 0$	-
	$\rho_w = constant $	
Gravity force	Gravitational effect is negligible.	-
	$\rho_w \bullet g = 0$	
	g is the gravitational	
	acceleration field.	
Free convection	$\mathbf{U_w} = 0$	The convective heat transfer
boundary		rate (Q _a)
conditions		$Q_a = h_a A_a (T_s - T_a)$, where h _a , A _a , T _s and T _a represent the
		convective heat transfer
		coefficient, surface area
		exposed to the ambient air,
		surface temperature exposed to
		air, and ambient air
		temperature, respectively.
		$h_a = 5 \text{ W/m}^2 \cdot \text{K}; T_a = 30^{\circ} \text{C}$
Battery cells	$\mathbf{U_w} = 0$	Heat generation in battery cells
3	- **	(ġ)
		See Eq. (7)
Radiation heat	$\mathbf{U_w} = 0$	The radiation heat transfer
transfer.		(Q _{rad}) is neglected.
		$Q_{rad} = 0$
Symmetrical plane	Just half of both the batte	ery and the cold plate domains are
of the battery pack		e and lower surfaces of the two
	halves are set as symmetr	ry (Fig. 1b).

each cold plate and is given by:

$$\begin{split} V_{CP} &= H_{CP} \bullet W_{CP} \bullet t_{CP} - t_{ch} \bullet \left(\left(n_{ch} \bullet W_{ch} \bullet L_{ch} \right) + \left(n_{ch} - 1 \right) \bullet \pi \right. \\ & \bullet \frac{r_2{}^2 - r_1{}^2}{2} + 2 \bullet W_{ch} \bullet \left(W_{CP} - \left(L_{ch} + r_2 + W_{s2} \right) \right) + W_w \bullet \left(n_{ch} - 1 \right) \\ & \bullet n_{int} \bullet W_{int} \right) \end{split}$$

where $H_{CP},\,W_{CP},$ and t_{CP} are the height, width, and thickness of the cold plate (m), respectively. t_{ch} is the depth of the minichannels (m). n_{ch} and n_{int} represent respectively the number of minichannels and V-shaped intersecting minichannels ($n_{ch}=14,\,n_{int}=7$). W_{ch} and W_{int} are the width of the minichannels and V-shaped intersecting minichannels, respectively (m). W_w represents the width of the minichannel wall (m), $W_w=(H_{CP}-n_{ch}\bullet W_{ch}-2\bullet W_{s1})/(n_{ch}-1)$. $W_{s1},\,$ and W_{s2} are the outside wall thicknesses, respectively (m), see Fig. 1. The symbols r_1 and $r_2,$ respectively, represent the inner and outer radius of the bent minichannel (m), $r_1=W_w/2,\,r_2=W_{ch}+W_w/2$. L_{ch} is the length of the straight minichannel (m), $L_{ch}=W_{CP}-2\bullet W_{s2}-2\bullet r_2$. Fig. 2 illustrates a schematic sketch of a single V-shaped intersecting minichannel to clarify the design parameters for the SMCCP-IVSMC design, where θ is the V-shape intersecting angle (°) and the distance δ is given by:

$$\delta = \left(\frac{0.5 \, W_{\scriptscriptstyle W} - R \cos \theta}{\sin \theta}\right) \tag{15}$$

3. Numerical validation and verification

A grid sensitivity test is carried out on the BTMS based on SMCCP-

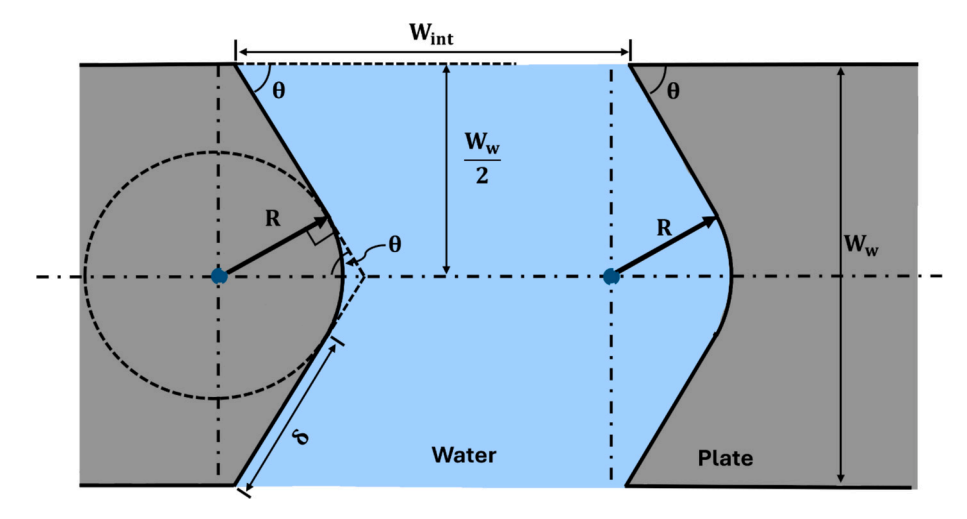


Fig. 2. Schematic diagram of the geometry of a single V-shape intersecting minichannel.

IVSMC illustrated in Fig. 1. Simulations are carried out in COMSOL Multiphysics® software (v.6.0) using free-tetrahedral grids with a number of elements ranging from 0.82×10^6 to 4.05×10^6 for a high discharge rate of 9C and an inlet flow velocity of 0.3 m/s. The software has been used to iteratively solve the partial differential equations (PDEs) of heat transfer and fluid flow using the finite element method (FEM) via an iterative solver. The finite element meshes consisted of numerous interconnected small elements with boundary edges that connected at endpoints called nodes. The 3D free tetrahedral mesh is the default mesh in COMSOL and is normally selected for its suitability for irregular geometries, including curved surfaces or the presence of small objects [103]. Because some BTMS domains have thin or irregular shapes, like V-shape regions, and due to the computational cost, all 3D computational domains of BTMS are discretised using various sizes of an unstructured free tetrahedral mesh with the help of the COMSOL preprocessor. High-quality meshes are essential for the efficiency and accuracy of the solution process in computational fluid dynamics (CFD) numerical simulation, whereas poor-quality meshes can significantly impact the stability and convergence of a finite element solver, as well as the accuracy of the PDE solution [104]. The mesh quality is a dimensionless factor that ranges from 0 to 1, where 1 represents high-quality meshes and 0 represents poor-quality meshes. The mesh quality (Q_{mesh}) for the tetrahedral element is computed using COMSOL Multiphysics for the laminar flow regime as follows [72]:

$$Q_{mesh} = \frac{72\sqrt{3} V}{\left(h_1^2 + h_2^2 + h_3^2 + h_4^2 + h_5^2 + h_6^2\right)^{1.5}}$$
 (16)

where V represents the volume and h_1 , h_2 , h_3 , h_4 , h_5 , and h_6 denote the edge lengths of the element; Q_{mesh} should exceed 0.1 to achieve an acceptable aspect ratio, edge ratio, and volume ratio, thus preventing stretched or distorted elements. The necessary steps for solving the numerical model in COMSOL Multiphysics software are presented as a flowchart in Fig. 3.

The effects of grid density on the maximum temperature as a function of time are shown in Fig. 4- it can be seen that the results are virtually indistinguishable. Further quantitative details are given in Table 4, where the PRE of the results of each grid with respect to those on the finest grid is determined using Eq. (17):

$$PRE(\%) = \left| \frac{Y_i - Y_{4.05 \times 10^6}}{Y_{4.05 \times 10^6}} \right| \tag{17}$$

where Y is the numerical results of the evaluated values of the physical parameters (in this case T_{max} and P_w) for a given number of elements (i).

Four timestep values (1.0 s, 2.0 s, 3.0 s, and 4.0 s) were used to assess the effect of the timestep – no significant variations can be discerned (see Fig. 5). Balancing the precision and computational cost, the current study used a free-tetrahedral grid with 2.36×10^6 elements with

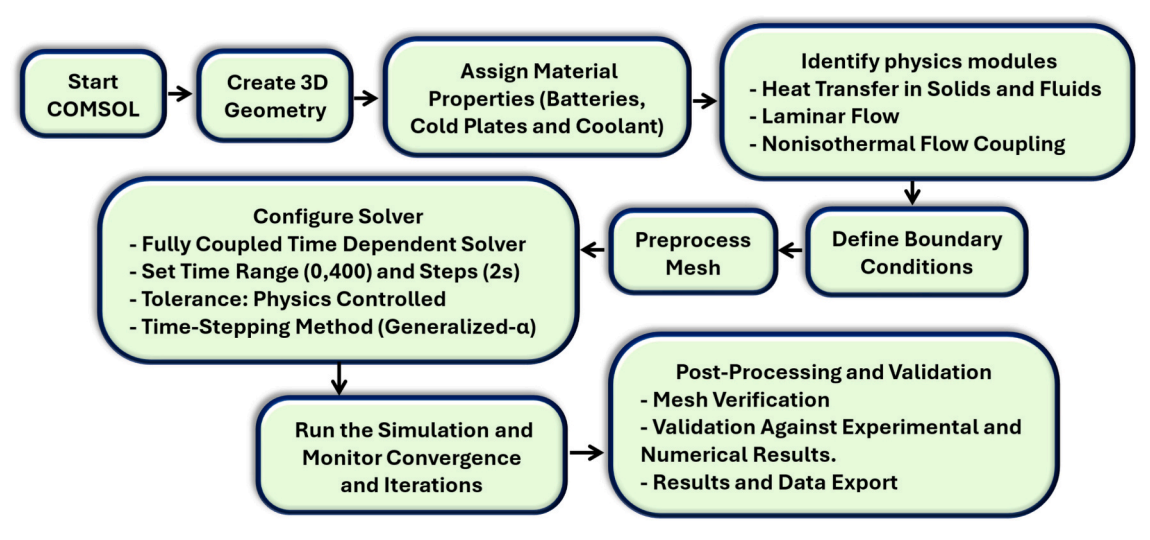


Fig. 3. Flowchart representing the necessary steps for solving the numerical model in COMSOL.

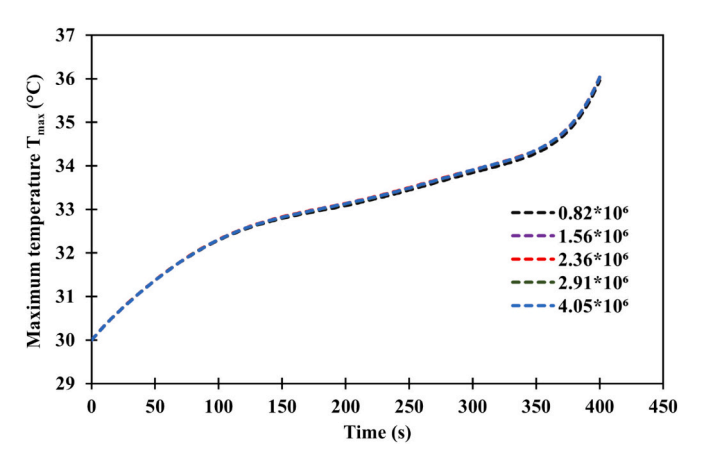


Fig. 4. Grid sensitivity of the battery maximum temperature throughout the discharge cycle.

Table 4Grid sensitivity results.

Number of elements	$T_{max}\ (^{\circ}C)$	$RPE(T_{max})\%$	$P_w(mW)$	RPE(P _w) %
0.82×10^6	35.96	0.221	0.71479	5.86
1.56×10^{6}	36.02	0.055	0.67862	0.51
2.36×10^{6}	36.04	0.000	0.67720	0.30
2.91×10^{6}	36.03	0.027	0.67707	0.28
4.05×10^{6}	36.04	0.000	0.67517	0.00

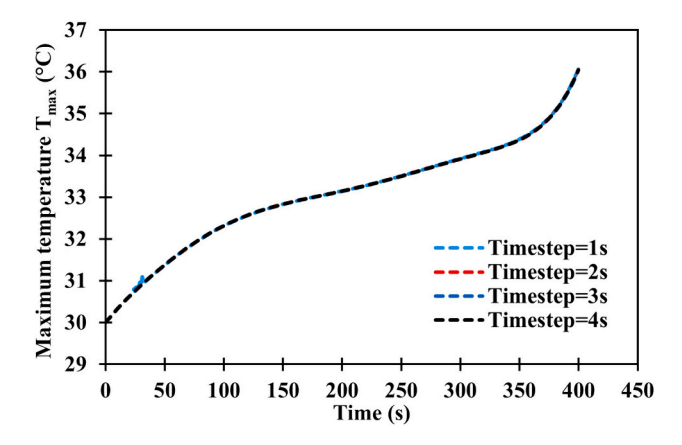


Fig. 5. Impact of timestep on the battery maximum temperature predictions throughout the discharge cycle.

corresponding mesh quality of 0.66, and a 2.0 s timestep.

A CFD model for BTMS based on SMCCP-IVSMC was constructed in COMSOL Multiphysics® (v.6.0) using a free-tetrahedral grid with 2.36×10^6 elements and a time-steps of (2.0 s) to validate the 3D fluid flow and heat transfer model developed here against the numerical simulations in ANSYS Fluent by Liu et al. [75] (case 4) when 8.0 Ah prismatic LiFePO_4 Li-ion batteries are fully discharged at a high discharge rate (9C). The obtained results were evaluated with respect to the maximum temperature of the battery and the water pumping power throughout a range of water inlet velocities from 0.1 to 0.5 m/s. Fig. 6 demonstrates that the results obtained here are in excellent agreement with those of Liu et al. [75], with a mean absolute percentage error (MAPE) of 0.02 % and 1.26 %, respectively. The MAPE is given by eq. (18) [23]:

$$MAPE = \frac{1}{N} \sum_{i=1}^{N} \frac{|Calculated\ value - Actual\ value|}{Actual\ value} \times 100\%$$
 (18)

where N represents the total number of evaluated points.

To further prove the reliability of the battery heat generation rate and the numerical model simulated in this study, Fig. 7 compares the numerical predictions of the present work with the numerical results and experimental findings reported in, Liu et al. [76] and Sheng et al. [82] respectively, during the discharge process Fig. 7. Comparison between the numerical of the present work, Liu et al. [76] and Sheng et al. [82] works for battery temperature during the discharge process at different high C-rates. There is very good agreement with both the previous sets of numerical and experimental results. As shown in the Fig. 7, the battery temperature gradually increases as the discharge rate rises from 3C to 9C. Accordingly, the maximum C-rate of 9C is chosen for further analysis in this work, because it reflects the worst-case scenario with the highest thermal load.

To further verify the accuracy of the present conjugate heat transfer and CFD model, the experimentally measured thermo-hydraulic performance, specifically the Nusselt number and apparent friction factor of a minichannel heat sink [105], is compared with the simulation results obtained using the present numerical approach, as shown in Fig. 8. It can be observed that the model predictions for the Nusselt number (*Nu*) and apparent friction factor (f) are in good agreement with the experimental data across various Reynolds numbers, which confirms the reliability and accuracy of the numerical approach employed in the present work.

4. Sensitivity analysis

The parameters having the greatest influence on the performance metrics are determined using sensitivity factors [106] in the form of:

$$S_{i} = \frac{\left(f_{max}\left(x_{i}\right) - f_{min}\left(x_{i}\right)\right)}{\sum_{j=1}^{n} \left(f_{max}\left(x_{j}\right) - f_{min}\left(x_{j}\right)\right)}$$

$$(19)$$

where $f_{max}(x_i)$, and $f_{min}(x_i)$ represent the maximum and minimum values of a single objective function (T_{max}, T_{σ}, P_w, or M_{CP}) when varying only one design variable x_i (such a $W_{\text{ch}},\,W_{\text{int}},\,\theta,\,R,$ or $W_{\text{s2}})$ over its full range. The term $\sum_{j=1}^{n} \left(f_{max}\left(x_{j}\right) - f_{min}\left(x_{j}\right)\right)$ is the sum of all differences between the maximum and minimum values of a single performance metric for all design variables. This sensitivity analysis is a simple and widely used approach to determine the impact of each input factor on the performance of the BTMS [106-112]. The sensitivity factors for all the design variables are displayed in Fig. 9, showing the relative impact of each design variable on the BTMS objective functions. The results of the sensitivity analysis demonstrated that W_{ch} has the most significant impact on $T_{max},\,T_{\sigma},\,P_{w},$ and $M_{CP},$ with sensitivity factors of 55.73 %, 76.24 %, 32.05 %, and 52.11 %, respectively. This is followed in descending order of significance by the V-shaped intersecting minichannels (W_{int}) and the V-shape intersecting angle (θ) comes next, with both the radius (R) and outside wall thickness (W₅₂) having only minor impacts. Accordingly, only the first three design variables (W_{ch}, W_{int}, and θ) are considered in the design optimization study.

5. Optimization methodologies

The validated battery thermal management model is used within a surrogate-enabled optimization of the cold plate's cooling system. The aim is to identify effective compromises between the various objectives for the design variables W_{ch} , W_{int} , and θ in the ranges $2.0 \leq W_{ch} \leq 5.0$, $1.0 \leq W_{int} \leq 5.0$, and $30^{\circ} \leq \theta \leq 60^{\circ}$, respectively. Optimal Latin hypercube sampling (OLHS) is used to generate 100 Design of Experiment (DoE) points that are uniformly distributed and efficiently cover the design space. Then, the high-fidelity BTM simulation model is used to compute T_{max} , T_{σ} , and P_{w} , at each DoE point, while the mass M_{CP} is determined via Eq. (12). Surrogate modeling is carried out using both Radial Basis Functions (RBFs) and Gaussian Process Regression (GPR) as a comparison. The former is used widely due to its simplicity and efficiency [113,114]. For example, a Gaussian RBFs- surrogate model

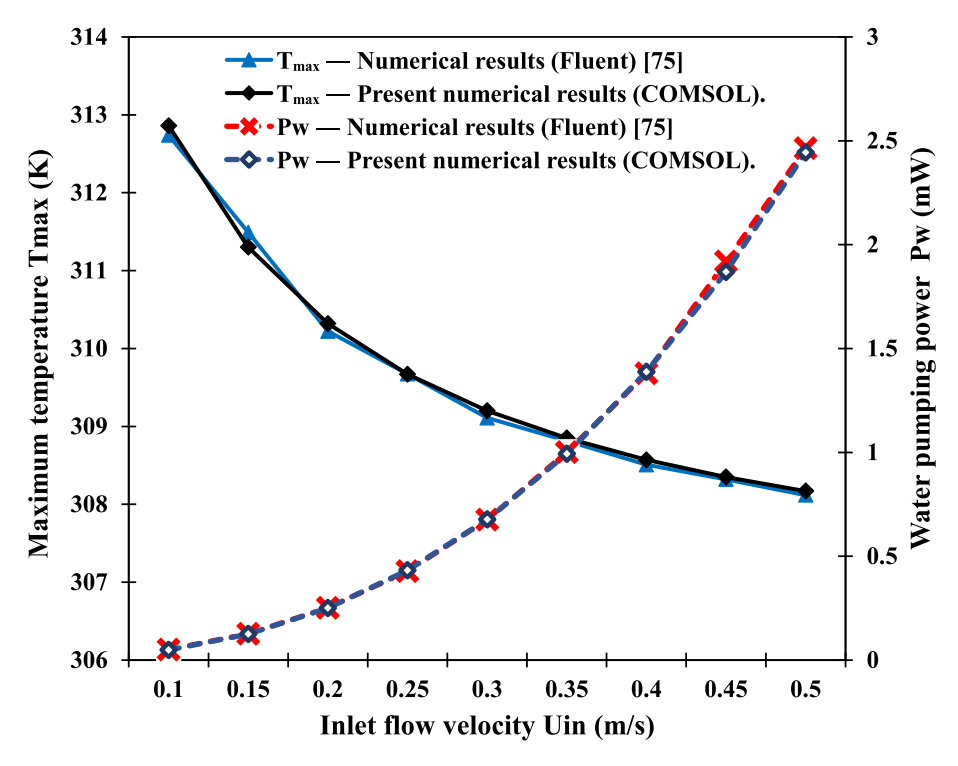


Fig. 6. A comparison between the present work's numerical results and those obtained by Liu et al. [75] for the maximum temperature of the battery and the water pumping power.

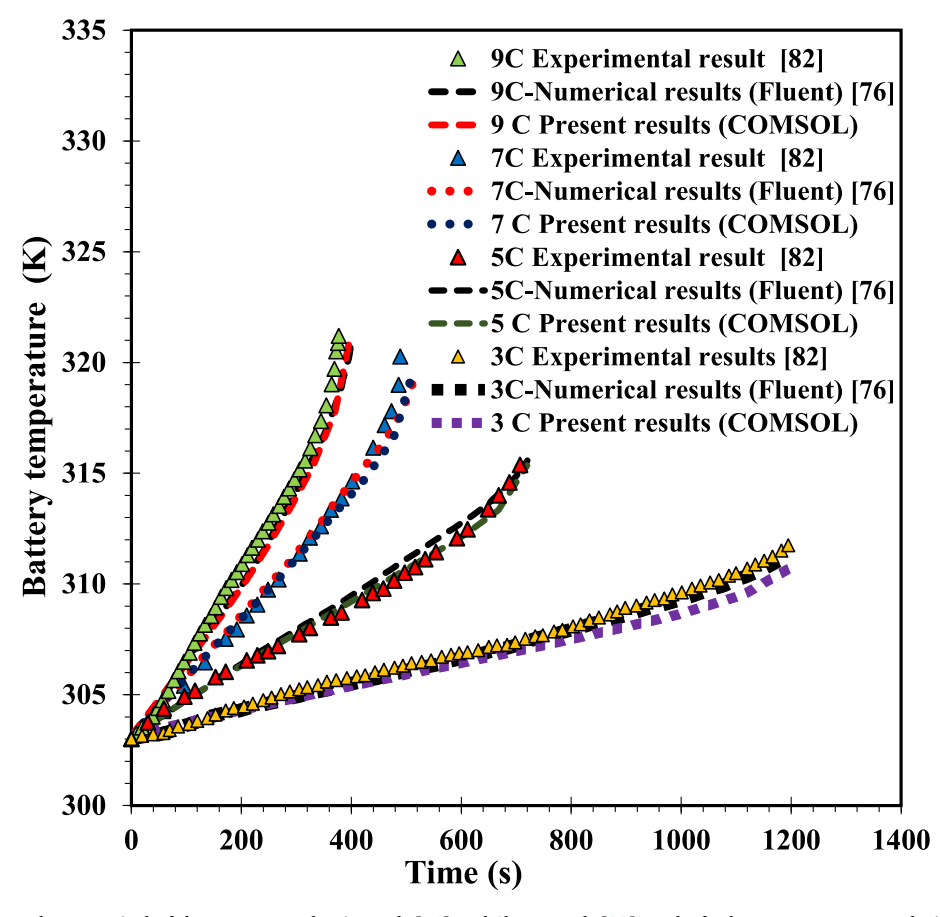


Fig. 7. Comparison between the numerical of the present work, Liu et al. [76] and Sheng et al. [82] works for battery temperature during the discharge process at different high C-rates.

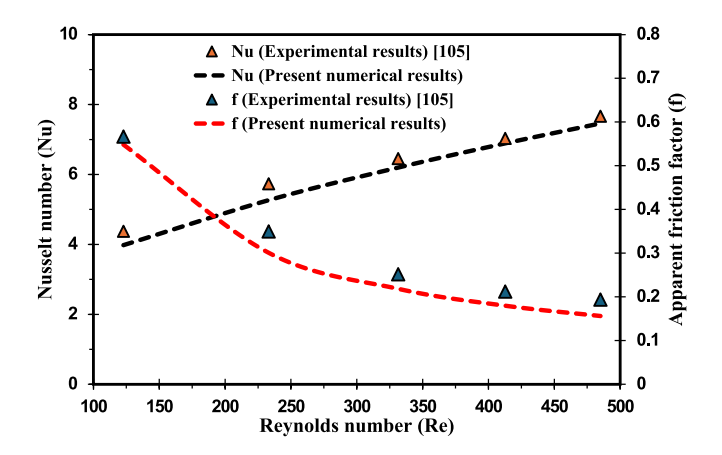


Fig. 8. Validation of the present simulation model with experimental results reported by Tikadar et al. [105] for the Nusselt number and apparent friction factor.

approximation $\hat{f}_J(x)$ for every objective function f_j at each design point $(x_i = [x_{(i,1)}, x_{(i,2)}, x_{(i,3)}])$ in the design space is computed by [115]:

$$\widehat{f}_{J}(\mathbf{x}) = \sum_{i=1}^{n} \lambda_{i} \varnothing(\|\mathbf{x} - \mathbf{x}_{i}\|), \varnothing = \exp\left(-\beta \bullet \|\mathbf{x} - \mathbf{x}_{i}\|^{2}\right)$$
(20)

Here, J is an acronym for objective functions (e.g. T_{max} , T_{σ} , and P_{w}) and n is the number of DoE points. λ_{i} is the vector of weights and β is the hyperparameter that controls the shape of the Gaussian RBF function. K-Fold Cross Validation (CV) with k=10 is used to optimize the hyperparameter β in relation to the Root Mean Square Error (RMSE):

$$RMSE = \sqrt{\frac{1}{N} \sum_{i=1}^{N} (f_i - \hat{f}_i)^2}$$
 (21)

where N is the total number of observed data points and \widehat{f}_i , and \widehat{f}_i are the actual observed and predicted values for the objective function, respectively. GPR is a very popular ML approach due to its inherent capabilities to account for uncertainties in the surrogate modeling process [116]. The GPR model approximates the function f(x) via two functions which represent the mean $\mu(x)$ and variance Z(x) [117] and can be expressed as follows:

$$F(\mathbf{x}) = \mu(\mathbf{x}) + Z(\mathbf{x}), \text{ where } Z(\mathbf{x}) \sim \mathcal{N}(0, \sigma^2)$$
(22)

The squared-exponential kernel, often known as the RBF kernel, is used in the present work to construct the correlation between the random variables (e.g. $Z(x^{(i)})$, $Z(x^{(j)})$), based on the distance between their relevant points in the design space ($x^{(i)}$ and $x^{(j)}$). The RBF kernel is chosen due to its capability for modeling complex nonlinear relationships, flexibility and popularity [118,119]. It is given by [120]:

$$\Sigma_{ij} = \sigma^2 \exp\left(-\sum_{l=1}^{n_d} \frac{\left(x_l^{(i)} - x_l^{(j)}\right)^2}{2\alpha_l^2}\right)$$
 (23)

where n_d is the number of the input design variables ($n_d=3$ in the present work) and α_l represents the length-scale parameter in the n_d – th coordinate direction. GPR-based surrogate modeling has been carried out using the Python GPy (v1.10.0) library. Further details on the ML-based GPR approach can be found in Martins and Ning [117].

The multi-objective problems were solved using a popular multi-objective evolutionary algorithm, namely the 3rd version of the differential evolution (DE) algorithm, generalized differential evolution (GDE3) [121]. This modifies the selection method of the basic DE to solve optimization problems with several objectives and constraints

[122]. The procedural steps of the GDE3 algorithm are clearly depicted in the flowchart given in Fig. 10. Additional information on the GDE3 algorithm can be found in Kukkonen and Lampinen [122].

Finally, the Technique for Order Preference by Similarity to an Ideal Solution (TOPSIS) approach, based on equally weighted and entropy-weighted methods, has been employed to find the best compromise solution (BCS) among the set of Pareto optimal solutions. Recently, TOPSIS has been extensively used and has proven to be a flexible and effective technique for multi-criteria decision-making analysis [123,124]. The main idea behind the TOPSIS method is that the best compromise solution is closest to the ideal point and farthest from the non-ideal point; when combined with the entropy-weight method to assign weights to each objective [125]. The main mathematical formulae of the entropy-weighted TOPSIS technique for finding the best compromise solutions (BCSs) are expressed as following steps [124,125]:

Step 1: Normalise the Pareto matrix obtained from the multiobjective optimisation. This normalisation process is as follows:

$$Y_{ij} = \begin{cases} \frac{y_{ij} - \min(y_{ij})}{\max(y_{ij}) - \min(y_{ij})}, & y_{ij} \text{ is} + \\ \frac{\max(y_{ij}) - y_{ij}}{\max(y_{ij}) - \min(y_{ij})}, y_{ij} \text{ is} - \end{cases}$$

$$(24)$$

where y_{ij} represents the elements of the Pareto matrix, which has n objective functions and m solutions. The (+) indicators refer to the objective functions that should be maximised, while the (-) indicators refer to the objective functions that should be minimised.

Step 2: The indicators are standardised as follows due to differences between the indicator units:

$$P_{ij} = \frac{Y_{ij}}{\sum_{i=1}^{m} Y_{ij}}$$
 (25)

Step 3: The entropy for each objective is computed as follows:

$$E_{j} = -\frac{1}{\ln(m)} \sum_{i=1}^{m} P_{ij} \ln(P_{ij}), (j = 1, 2, \dots, n) (\text{If } P_{ij} \approx \text{Ouse } P_{ij} \ln(P_{ij}) = 0)$$
(26)

Step 4: The entropy weight for each objective is computed as follows:

$$w_{j} = \frac{1 - E_{j}}{\sum_{j=1}^{n} (1 - E_{j})}$$
 (27)

Step 5: The ideal and non-ideal points are identified, respectively, as follows:

$$Y^{+} = \left(\max_{i} Y_{i1}, \max_{i} Y_{i2}, \dots, \max_{i} Y_{in}\right)$$
 (28)

$$Y^{-} = \left(\min_{i} Y_{i1}, \min_{i} Y_{i2}, \dots, \min_{i} Y_{in} \right)$$
 (29)

Step 6: The distances of Pareto solutions to ideal and non-ideal points for the entropy-weighted TOPSIS are calculated as follows, respectively:

$$D_{i}^{+} = \sqrt{\sum_{i=1}^{m} w_{j}^{2} \left(Y^{+} - Y_{ij}\right)^{2}}$$
 (30)

$$D_{i}^{-} = \sqrt{\sum_{i=1}^{m} w_{j}^{2} (Y^{-} - Y_{ij})^{2}}$$
 (31)

Note that the w^2 will not be included in eqs. (30) and (31) if the general TOPSIS method is used, since all objectives are considered to

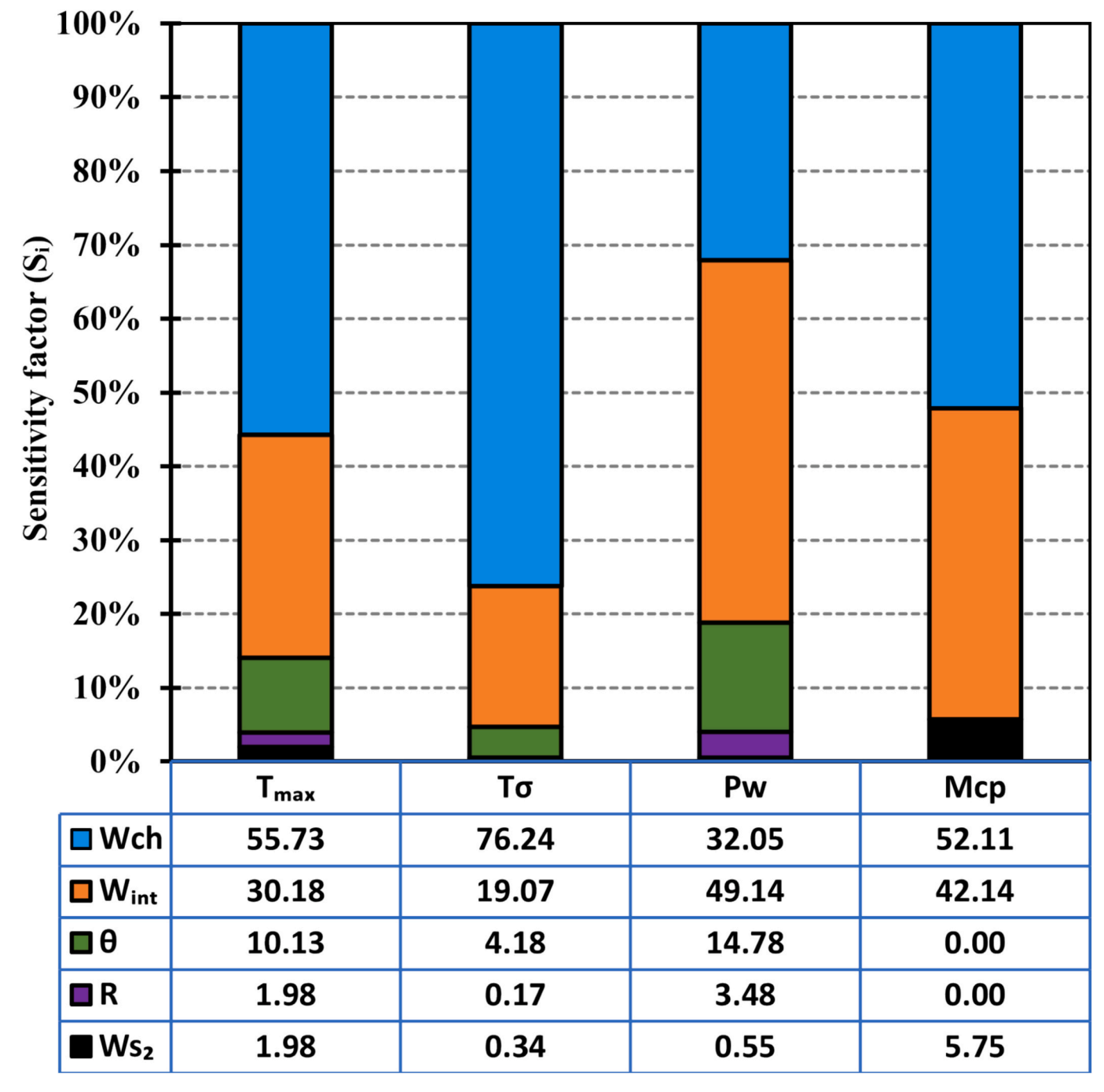


Fig. 9. Sensitive analysis of $T_{max},\,T_{\sigma},\,P_{w},$ and $M_{CP}.$

have equal weight.

Step 7: The evaluation factors (also called closeness coefficients) for each Pareto solution are computed as follows:

$$C_i = \frac{D_i^-}{D_i^+ + D_i^-} \tag{32}$$

when the closeness coefficient (C_i) is much closer to one, it indicates that its corresponding Pareto optimal solution is the most effective compromise solution, being nearer to the ideal point and farther from the non-ideal point.

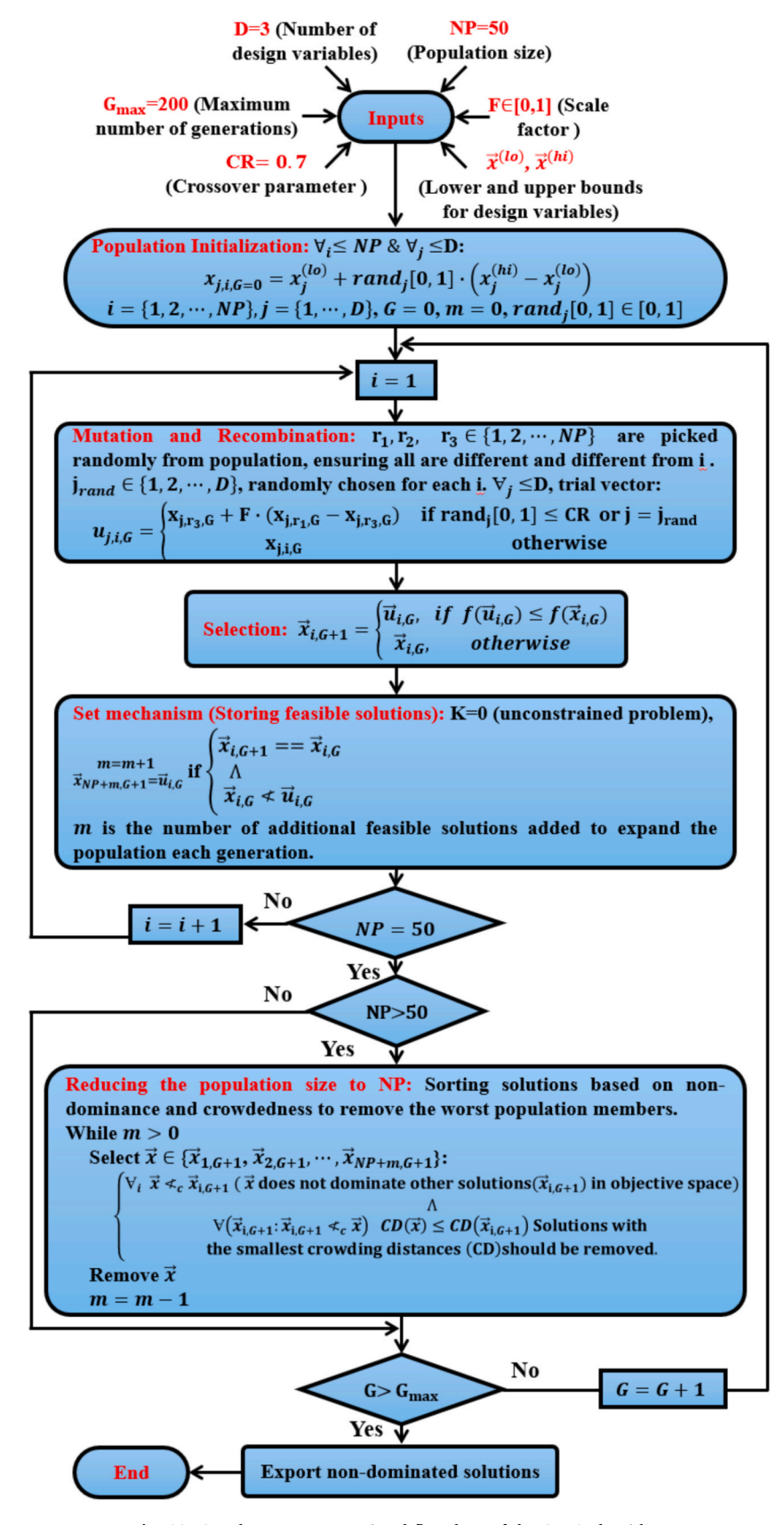
Step 8: The best compromise solutions for two, three, and four objectives optimisation are respectively calculated as follows:

$$BCS_2 = \max_i C_i \tag{33}$$

$$BCS_3 = \max_i C_i \tag{34}$$

$$BCS_4 = \max_i C_i \tag{35}$$

Fig. 11 shows the flowchart of the multi-objective optimization process, illustrating the integration of ML and GDE3 algorithm with the TOPSIS approaches to identify BCSs.



 $\textbf{Fig. 10.} \ \ \textbf{Step-by-step computational flowchart of the GDE3 algorithm}.$

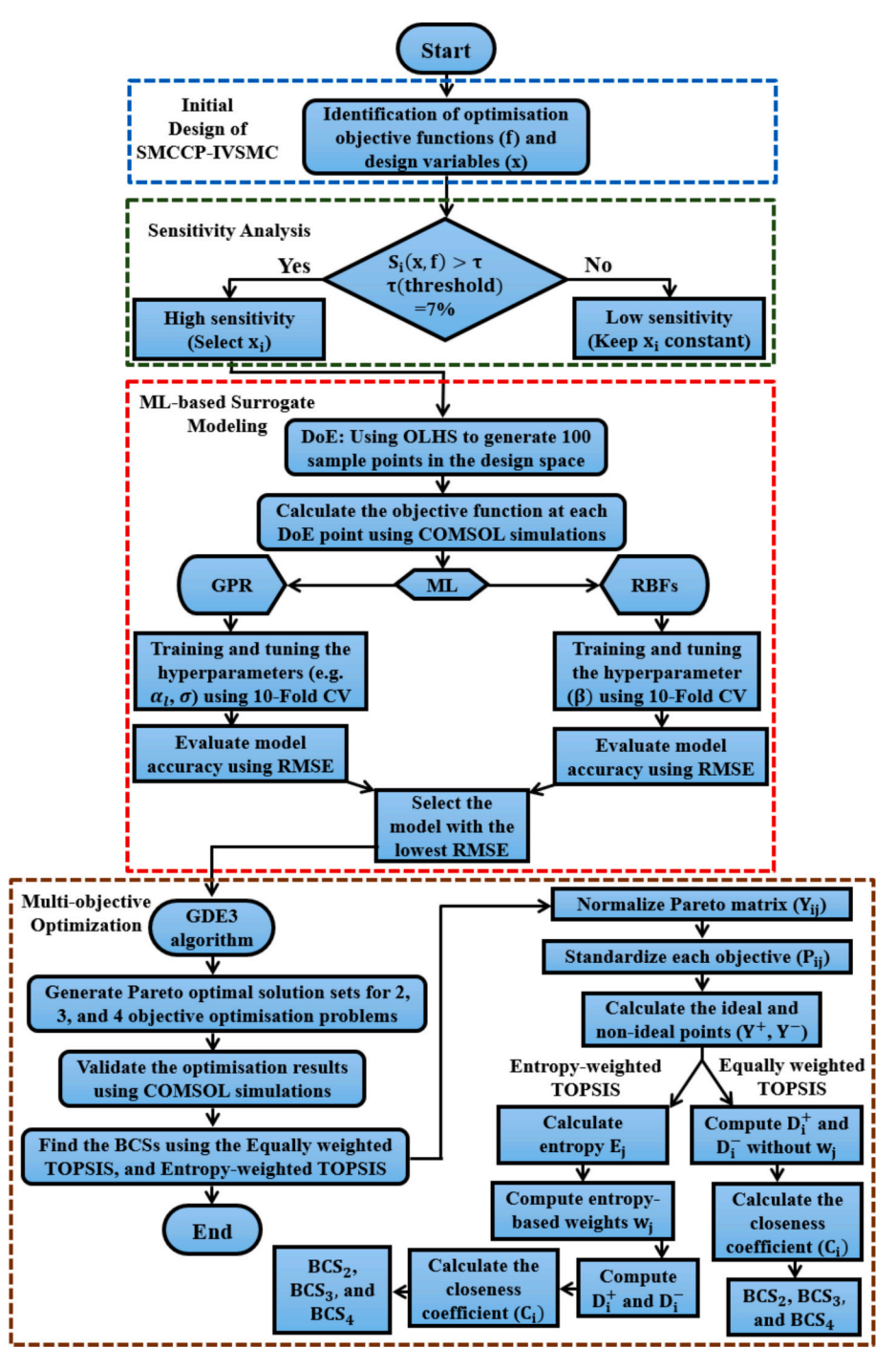


Fig. 11. Multi-objective optimization process integration ML with GDE3 and TOPSIS for finding BCSs.

Table 5Benchmark design of the BTMS.

	Acronym	Benchmark design
Design variables	W _{ch} (mm)	3.50
	W_{int} (mm)	2.00
	0 (°)	45.00
Objective functions	$\mathbf{T_{max}}$ ($^{\circ}\mathbf{C}$)	35.96
	$P_{\mathbf{w}}$ (mW)	0.68
	$T_{\sigma}(K)$	1.034
	M _{CP} (g)	54.12

6. Results and discussion

6.1. Benchmark design performance

To systematically demonstrate and evaluate the effectiveness of the multi-objective optimisation carried out in this work, it is essential to establish a baseline benchmark design performance. The BTMS benchmark design has been chosen based on previous simulation results conducted by Liu et al. [75], whereby the battery's maximum temperature and pumping power were extracted from Fig. 6 (case 4) in their study at an inlet flow velocity of 0.3 m/s. The other related performance metrics of the benchmark design, including the mass of each cold plate and the battery's temperature standard deviation, have been computed

in the present work based on their original design. This BTMS benchmark design details are shown in Table 5.

6.2. Machine learning (ML) hyperparameters calibration

Fine-tuning the hyperparameters of ML approaches is essential in optimizing the learning process, to avoid overfitting, and generate accurate predictions of the objective function. Fig. 12a, b, and c display the RMSE tuning curves for the β parameter in Gaussian RBF regression using 10-Fold cross-validation. The values of the β corresponding to the lowest RMSEs are 1.227, 1.619 and 0.492 for the $T_{max},\,T_{\sigma},$ and P_{w} RBF models, respectively.

The maximum likelihood approach [117] is used to calibrate the hyperparameters of the $T_{max},\,T_{\sigma},$ and P_{w} GPR models by maximizing the probability of observing the data f. These are shown in Table 6.

Table 7 displays the RMSE for each calibrated ML model obtained throughout the K-fold CV for each objective function. A comparison between the two methods is shown in Fig. 13a and Fig. 13b for $P_{\rm w}.$ Generally, the surrogate models from both ML methods are similar to one another. The GPR method performs better for all objectives and will be used in all subsequent results.

6.3. Single-objective optimization

The single-objective optimizations are straightforward since the global minima are located on the edges of the design space. Table 8 lists the global minima for each objective function along with the corresponding design variables used in the GPR models. Table 8 also displays the values of the other objective functions when they are calculated using optimum points obtained through single objective optimization. Note that when T_{max} is minimised, P_w and M_{CP} are relatively large, and when P_w is minimised, the values of all other objectives T_{max} , T_σ and M_{CP} have extremely high values. This indicates that it will be beneficial to perform multi-objective optimizations to explore the available compromises between the objectives.

Table 6Main configuration parameters for GPR ML models.

Model	No. of restarts optimizer	Length scale (α)	Length scale range
T _{max}	10	3	(0.1, 10)
T_{σ}	10	3	(0.1, 10)
$\mathbf{P_w}$	10	3	(0.1, 10)

Table 7
K-fold CV RMSE for each ML model.

ML model	RMSE	
	RBF	GPR
T _{max} (°C)	0.2071	0.0281
$T_{\sigma}(K)$	0.0199	0.0051
P_w (mW)	0.0547	0.0114

6.4. Multi-objective design optimization

Two-dimensional Pareto fronts are constructed using the GPR surrogate models to demonstrate the available trade-offs between T_{max} , T_{σ} , P_{w} , and M_{CP} . The GDE3 algorithm employed here is available in the pymoode Python package (v0.2.6). The parameters used for setting the GDE3 algorithm are given in Table 9.

Referring to Fig. 14a to Fig. 14f, the Pareto Fronts and design of experiment points are displayed between the objective function pairs: P_w against T_{max} , M_{CP} against T_{max} , M_{CP} against P_w , P_w against T_σ , M_{CP} against T_σ , and T_{max} against T_σ , respectively. These plots illustrate the relationship between two conflicting objectives, through non-dominated points, where an increase in one objective causes a decrease in the other. A number of significant variations are identified. For instance, in Fig. 14a, decreasing T_{max} from 39 $^{\circ}$ C to 35 $^{\circ}$ C results in P_w increasing from around 0.25 mW to 2.2 mW. However, the increase in T_{max} from around 35.0 $^{\circ}$ C to 36.5 $^{\circ}$ C in Fig. 14b causes M_{CP} to decrease from around 50.0 g to 41.5 g. Similarly, in Fig. 14c, an increase in P_w from 0.25 mW to 0.55 mW enables M_{CP} to be decreased from approximately 51.5 g to 42 g. The decreasing T_σ from about 1.5 K to 0.9 K in Fig. 14d

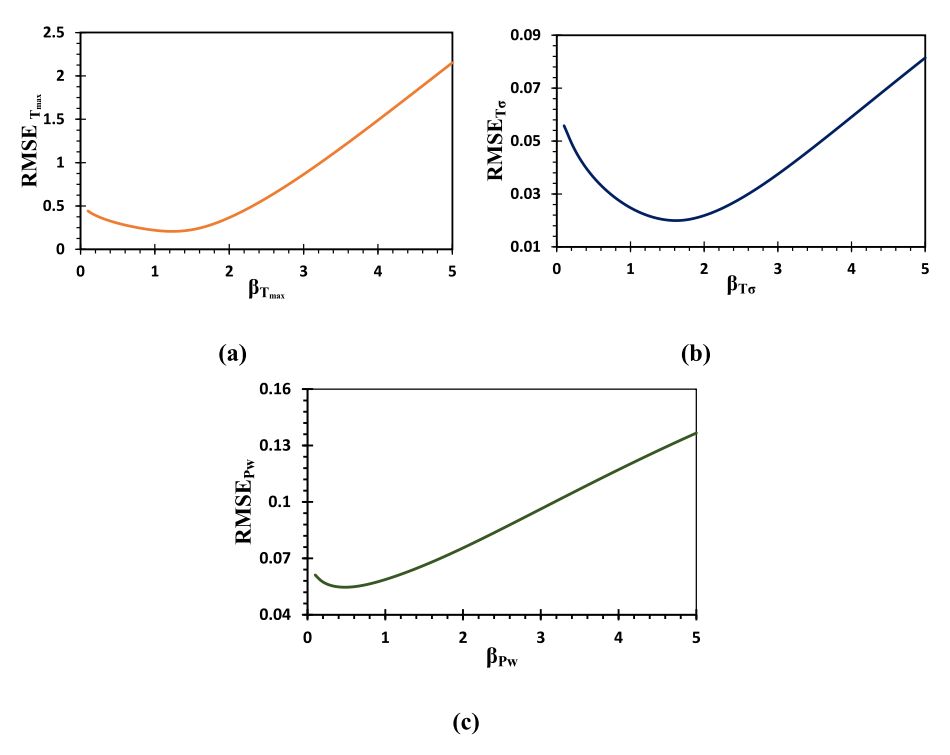


Fig. 12. The RMSE calibration curves for the β hyperparameter: (a) $T_{max},$ (b) $T_{\sigma},$ and (c) $P_{w}.$

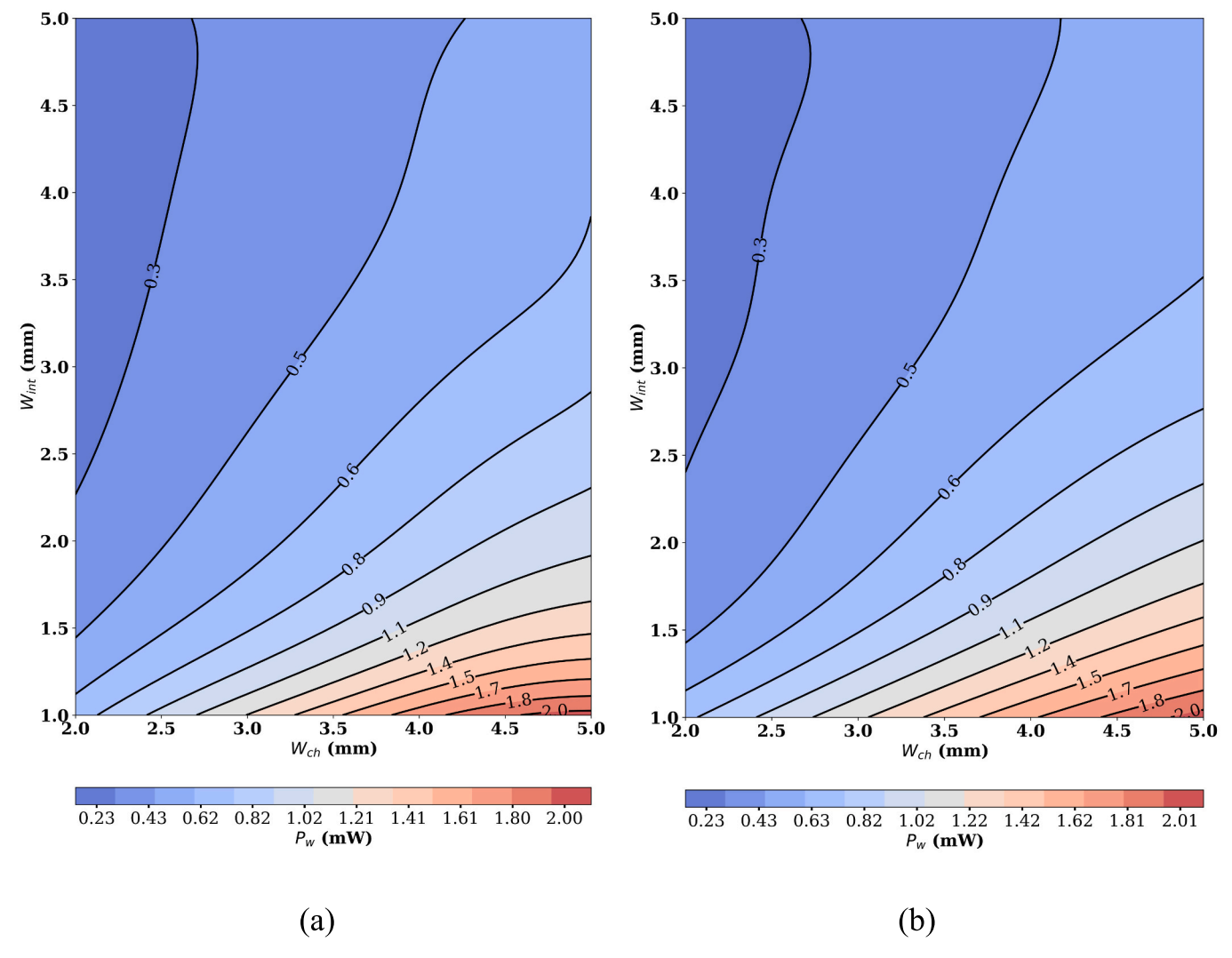


Fig. 13. Surrogate models of the P_w using the RBF and GP approaches; the third design variable, θ , is fixed at 45°: (a) RBF regression, and (b) GPR.

Table 8Single objective optimization using the GPR model.

Objective function	Global minima	W _{ch} (mm)	W _{int} (mm)	0 (°)	$T_{max}(^{\circ}C)$	$T_{\sigma}\ (K)$	$P_{w}\;(mW)$	$M_{CP}\left(g\right)$
$T_{max}(^{\circ}C)$	34.97	5.00	1.00	39.67	34.97	0.9175	2.1070	49.476
$T_{\sigma}(K)$	0.8914	5.00	1.00	53.35	35.01	0.8914	1.9519	49.476
$P_{w}(mW)$	0.2134	2.00	3.46	60.00	38.92	1.4992	0.2134	55.863
$\mathbf{M_{CP}}(\mathbf{g})$	41.787	5.00	5.00	54.56	36.40	1.0101	0.5319	41.787

Table 9Setting parameters for the GDE3 algorithm.

Setting parameter	Value
Variant	"DE/rand/1/bin"
Size of the population in each generation	50
Maximum number of generations	200
Scale factor or mutation parameter (F)	(0.0, 1.0)
Crossover parameter (Cr)	0.7

would result in P_w increasing from around 0.25 mW to 2.0 mW. However, in Fig. 14e, M_{CP} drops from roughly 50.0 g to 41.5 g as a result of the increase in T_σ from around 0.87 K to 1.00 K. However, the Pareto front of T_{max} against T_σ in Fig. 14f indicates that the minima of maximum temperature and temperature standard deviation are strongly related to one another.

The accuracy of the Pareto Fronts generated by the GDE3 method is confirmed by comparing some of the optimal Pareto points with their corresponding CFD predictions. Table 10 compares the objective function values for the chosen Pareto points from Fig. 14a with the corresponding CFD results. In general, the agreement is generally very good, although the errors in $P_{\rm w}\,$ do grow as $P_{\rm w}\,$ increases.

Fig. 15 shows a 2D surface representation of the Pareto surface for T_{max} and M_{CP} . The colour gradient corresponds to the pumping power, ranging from 0.210 mW (dark blue) to 2.720 mW (red). This visualization highlights how changes in the temperature and mass influence pumping power: regions with lower pumping power are represented in blue, indicating more energy-efficient designs. The plot reveals distinct trade-offs: increasing the cold plate mass or the maximum temperature generally leads to lower pumping power, suggesting that achieving energy efficiency may require either heavier designs or higher operating temperatures. The colour transitions also emphasise the nonlinear

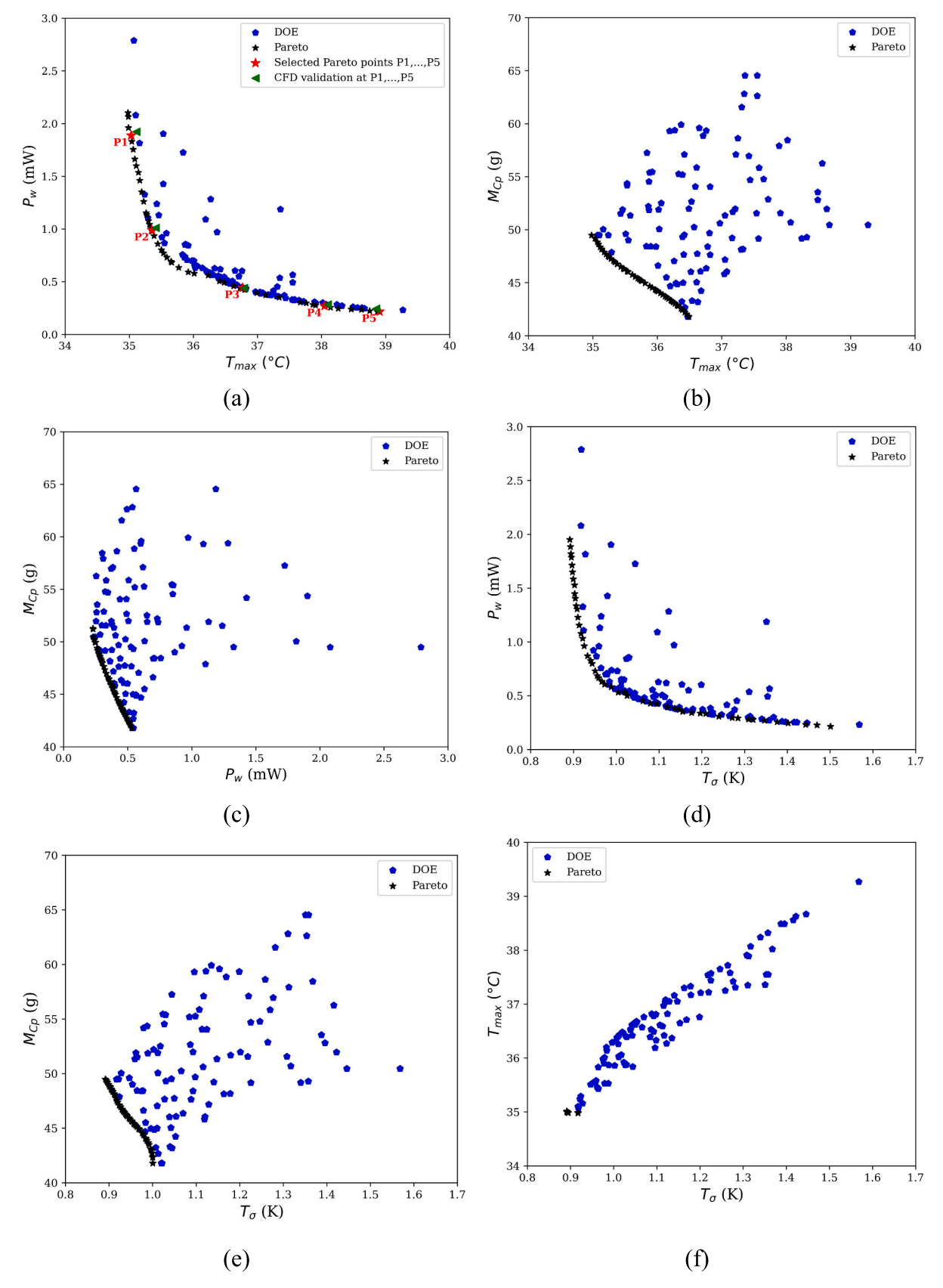


Fig. 14. Pareto Fronts obtained using the GPR ML approach: (a) P_w against T_{max} ; (b) M_{CP} against T_{max} ; (c) M_{CP} against P_w ; (d) P_w against T_σ ; (e) M_{CP} against T_σ ; (f) T_{max} against T_σ .

Table 10Verification of the objective function values for some optimal Pareto points from Fig. 14a with their corresponding CFD results.

Design variables (mm)		$T_{max}(^{\circ}C)$	$T_{max}(^{\circ}C)$		$P_{\mathbf{w}}\;(mW)$		Error %	
W_{ch} (mm)	$W_{int}\;(mm)$	θ (°)	Pareto	CFD	Pareto	CFD	T _{max}	$P_{\rm w}$
5.000	1.058	57.034	35.029	35.109	1.888	1.923	0.228	1.820
4.970	2.330	30.032	35.354	35.411	0.9905	1.011	0.161	2.028
3.718	4.253	34.441	36.767	36.790	0.4432	0.440	0.063	0.727
2.150	3.308	38.685	38.049	38.098	0.2719	0.284	0.129	4.261
2.001	3.541	59.477	38.905	38.850	0.2181	0.243	0.142	10.247

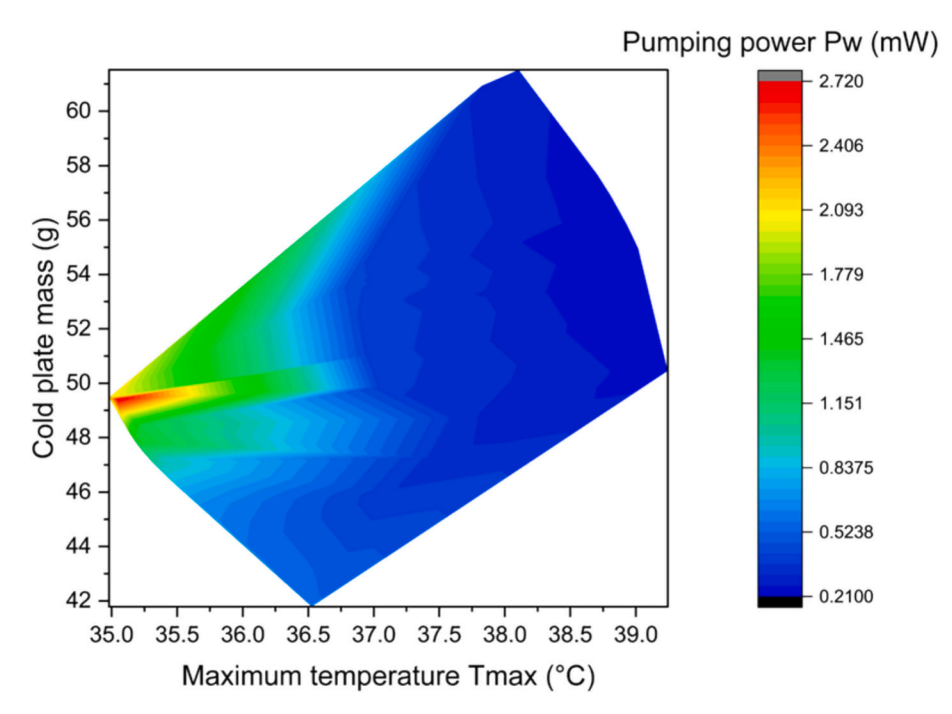


Fig. 15. Pareto surface distribution to analyse the trade-offs between T_{max} , P_{w} , and M_{CP} .

nature of the relationships among the objectives, highlighting regions where small changes in one parameter can lead to significant variations in the other two. Additionally, the concentration of red near the lower mass values and lower T_{max} values suggests these regions are more sensitive to variations, making them critical for further exploration or optimization. The graph also enables to implicitly identify feasible and

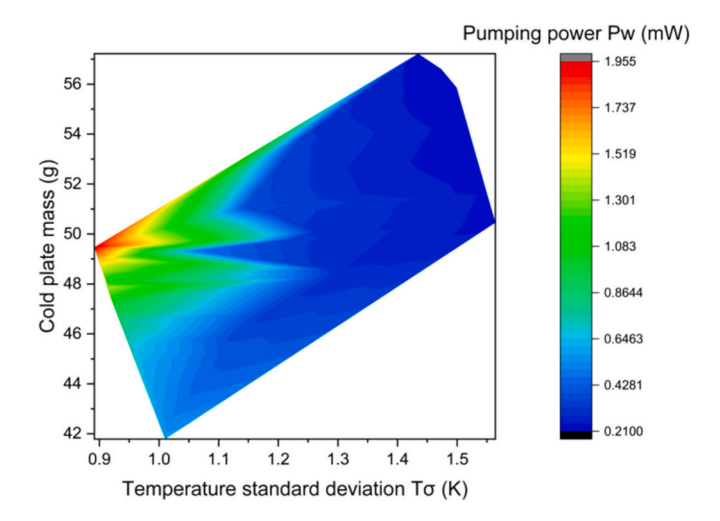


Fig. 16. Pareto surface distribution to analyse the trade-offs between $T_{\sigma},\,P_{w},$ and $M_{CP}.$

infeasible design spaces, enabling designers to focus on those areas that balance efficiency and performance without exceeding practical constraints.

The Pareto surface in Fig. 16 shows a 2D surface representation of the trade-offs between T_σ , M_{CP} , and P_w . It shows that increasing the cold plate mass or the battery's temperature standard deviation generally results in lower pumping power, indicating that attaining energy efficiency may demand either heavier designs or accepting an uneven temperature distribution. The colour transitions also point out the nonlinear relationships between these objectives, which show regions where slight changes in one objective can result in substantial variations in the other two. Furthermore, the red region next to the lower T_σ and relatively low M_{CP} indicates that performance in this region is particularly sensitive to variations, making it worthy of further exploration and optimization.

The accuracy of the Pareto optimal surface in Fig. 15 is demonstrated by comparing some of its optimal points with their corresponding CFD results in Table 11, which also shows the compromises available between the competing objectives. For instance, choosing design 1 instead of 12 in Table 11 significantly lowers the battery maximum temperature from 39.24 °C to 35.05 °C, albeit with an order of magnitude increase in pumping power, from 0.23 mW to 2.62 mW, which adversely affects the EV's driving range. This is also associated with a slightly reduced cold plate mass, from 50.46 g to 49.33 g, which is advantageous for both the driving range and manufacturing costs. Choosing design 7 instead of design 12 significantly reduces the mass by around 17.2 %, from 50.46 g to 41.79 g, but more than doubles the pumping power from 0.23 mW to

Table 11
Validation of the objective functions for some Pareto points from Fig. 15 with their corresponding CFD results.

Design	Design va	riables		$T_{max}(^{\circ}C)$		$P_{w}\;(mW)$		$\mathbf{M}_{\mathbf{CP}}$ (g)		error %		
	W _{ch} (mm)	W _{int} (mm)	θ (°)	Pareto	CFD	Pareto	CFD	Pareto	analytical	T_{max}	$P_{\rm w}$	M _{CP}
1	5.00	1.077	30.00	35.048	35.074	2.6240	2.5393	49.329	49.329	0.073	3.337	0.00
2	5.00	1.27	30.00	35.064	35.109	2.2303	2.0485	48.943	48.943	0.127	8.873	0.00
3	4.99	2.01	30.00	35.231	35.220	1.2327	1.1937	47.527	47.527	0.032	3.267	0.00
4	4.87	2.43	30.00	35.406	35.449	0.9257	0.9588	47.220	47.220	0.122	3.451	0.00
5	4.99	3.47	30.27	35.911	36.135	0.6027	0.6317	44.725	44.725	0.621	4.585	0.00
6	4.99	3.98	30.00	36.114	36.264	0.5678	0.5819	43.739	43.739	0.413	2.416	0.00
7	5.00	5.00	42.37	36.526	36.462	0.5338	0.5305	41.788	41.788	0.176	0.636	0.00
8	3.12	2.75	49.17	36.816	36.804	0.4338	0.4352	53.619	53.619	0.032	0.327	0.00
9	3.08	4.97	49.64	37.500	37.529	0.3295	0.3374	47.242	47.242	0.076	2.355	0.00
10	2.00	1.85	59.99	38.105	38.114	0.2856	0.3088	61.521	61.521	0.023	7.518	0.00
11	2.03	3.83	40.98	38.550	38.561	0.2453	0.2503	54.409	54.409	0.028	1.966	0.00
12	2.00	5.00	59.99	39.243	39.295	0.2315	0.2322	50.455	50.455	0.131	0.273	0.00

0.53 mW, both of which influence the EV driving range. The battery maximum temperature also reduces significantly from $39.24~^{\circ}\text{C}$ to $36.53~^{\circ}\text{C}$, improving battery safety. Lastly, choosing design 1 instead of design 7 lowers T_{max} from $36.53~^{\circ}\text{C}$ to $35.05~^{\circ}\text{C}$, which is helpful for battery safety. However, both the pumping power and the mass of the material for each cold plate increase considerably (from 0.53~mW to 2.62~mW and 41.79~g to 49.33~g, respectively), increasing the operating and manufacturing costs significantly.

6.5. TOPSIS optimization results

The equally-weighted and entropy-weighted TOPSIS techniques have been employed to identify the best compromise solutions from the optimal Pareto sets, helping designers and decision-makers to make well-informed and precise choices. Accordingly, these techniques have been applied to several multi-objective optimisation cases involving two, three, and four objective functions. Tables 12–14 show the best compromise solutions (BCSs) with the highest closeness coefficients (C_i) for two-, three-, and four-objective problems, using the equally-weighted TOPSIS method, which treats all objectives as equally weighted, and the entropy-weighted TOPSIS method, which assigns different weights to the objectives. These tables list the highest closeness coefficients for various combinations of the objective functions that provide the most balanced optimal solution among a set of competing trade-offs.

The closeness coefficients corresponding to each of the optimal Pareto sets for the four-objective optimisation case (T_{max} , P_w , T_σ , and

 M_{CP}), calculated using both the general TOPSIS method and the entropy-weighted TOPSIS method, are listed in the Appendix, Tables Table A.1 and Table A.2, respectively. These two tables rank the Pareto-optimal solutions for the 4-objective case in descending order of C_i , starting from the highest to the lowest, using the two TOPSIS methods.

Four optimum candidate designs and two solutions represent the top rankings of BCSs obtained from the two TOPSIS methods, which are chosen and compared with the BTMS benchmark design in Table 15. Compared to the benchmark design, the candidate optimisation results indicate that the battery's maximum temperature can be reduced from 35.96 °C to 34.98 °C by 2.7 %, the pumping power can be substantially lowered from 0.68 mW to 0.213 mW by 68.7 %, the battery's temperature standard deviation can be effectively reduced from 1.034 K to 0.891 K by 13.8 %, and the mass of each cold plate can be beneficially lowered from 54.12 g to 41.79 g by 22.8 %. The effectiveness of the optimization approach is further demonstrated by the identification of design 5 (the top-ranked BCS using equally weighted TOPSIS), which enables all four competing objectives to be reduced simultaneously.

7. Conclusions

There is a pressing need to extract the maximum performance from Li-ion EV batteries to maximise driving range and safety and minimise operating and manufacturing costs. To this end, a novel machine learning-enabled multi-objective optimization methodology for cold plates with intersecting V-shaped mini-channels for Li-ion BTMS has been developed, where the conjugate heat transfer model has been

Table 12BCSs and weights for two-objective optimization using the two different weighted TOPSIS methods.

TOPSIS method	2-objectives optimization	Design variabl	les		BCS		C_i	Objective	weights
		W _{ch} (mm)	W _{int} (mm)	θ (°)	Objective 1	Objective 2		$\overline{\mathbf{w}_1}$	\mathbf{w}_2
Equally weighted	P _w vs. T _{max}	5.00	3.18	30.00	P _w (mW)	T _{max} (°C)	0.7895	0.500	0.500
					0.6496	35.72			
Entropy-weighted		5.00	3.03	30.00	0.6856	35.66	0.7944	0.453	0.547
Equally weighted	M _{CP} vs. T _{max}	5.00	2.58	30.00	$M_{CP}(g)$	$T_{max}(^{\circ}C)$	0.5388	0.500	0.500
					46.43	35.45			
Entropy-weighted		5.00	2.28	30.00	47.02	35.32	0.5536	0.479	0.52
Equally weighted	$\mathbf{M}_{\mathbf{CP}}$ vs. $\mathbf{P}_{\mathbf{w}}$	3.26	5.00	54.14	M_{CP} (g)	$P_w(mW)$	0.5531	0.500	0.500
					46.65	0.3432			
Entropy-weighted		3.19	5.00	54.06	46.83	0.3374	0.5555	0.492	0.508
Equally weighted	P_{w} vs. T_{σ}	5.00	3.81	46.77	$P_w (mW)$	T_{σ} (K)	0.8166	0.500	0.500
					0.5777	0.985			
Entropy-weighted		5.00	3.81	46.77	0.5777	0.985	0.8226	0.445	0.555
Equally weighted	M_{CP} vs. T_{σ}	5.00	2.25	30.00	$M_{CP}(g)$	$T_{\sigma}(K)$	0.5084	0.500	0.500
					47.08	0.923			
Entropy-weighted		4.99	1.00	53.36	49.47	0.891	0.5684	0.432	0.568
Equally weighted	T_{max} vs. T_{σ}	5.00	1.00	55.54	$T_{max}(^{\circ}C)$	T_{σ} (K)	0.8211	0.500	0.500
					34.98	0.894			
Entropy-weighted		5.00	1.00	55.54	34.98	0.894	0.8452	0.400	0.60

Table 13
BCSs and weights for three-objective optimization using the two different weighted TOPSIS methods.

TOPSIS method	3-objectives optimization	Design variables			BCS C_i		Ci	Objective	e weights		
		W _{ch} (mm)	W _{int} (mm)	θ (°)	Objective 1	Objective 2	Objective 3		$\overline{\mathbf{w}_1}$	W ₂	w ₃
Equally weighted	$M_{\text{CP}},T_{\text{max}},\text{and}P_{\text{w}}$	5.00	3.51	30.00	M _{CP} (g) 44.65	T _{max} (°C) 35.88	P _w (mW) 0.5976	0.8255	1/3	1/3	1/3
Entropy-weighted		5.00	2.76	30.00	46.09	35.53	0.7773	0.8346	0.262	0.503	0.235
Equally weighted	$M_{CP},T_{\sigma},$ and P_{w}	5.00	5.00	54.19	M _{CP} (g) 41.78	$T_{\sigma}(K)$ 1.009	P_w (mW) 0.5315	0.8580	1/3	1/3	1/3
Entropy-weighted		5.00	5.00	54.19	41.78	1.009	0.5315	0.8610	0.345	0.379	0.275

Table 14BCSs and weights for four-objective optimization using the two different weighted TOPSIS methods.

TOPSIS	4-objectives	Design	variables		BCS				C_i	Objecti	rive weights		
method	optimization	W _{ch} (mm)	$\begin{matrix} W_{int} \\ (mm) \end{matrix}$	θ (°)	Objective 1	Objective 2	Objective 3	Objective 4		\mathbf{w}_1	\mathbf{w}_2	w ₃	W ₄
Equally weighted Entropy- weighted	$T_{max}, T_{\sigma}, P_{w},$ and M_{CP}	5.00 5.00	3.46 2.64	30.00 30.00	T _{max} (°C) 35.86 35.47	T _σ (K) 0.973 0.937	P _w (mW) 0.604 0.827	M _{CP} (g) 44.76 46.33	0.8373 0.8688	0.250 0.381	0.250 0.314	0.250 0.156	0.250 0.149

Table 15
Candidate optimum designs of the BTMS.

	Acronym	Bound	Benchmark design	Optimum candidate design (1)	Optimum candidate design (2)	Optimum candidate design (3)	Optimum candidate design (4)	BCS equally weighted TOPSIS design (5)	BCS entropy- weighted TOPSIS design (6)
Design	$W_{ch}\ (mm)$	2–5	3.50	5.00	2.00	5.00	5.00	5.00	5.00
variables	$W_{int} (mm)$	1–5	2.00	1.00	3.46	1.00	5.00	3.46	2.64
	0 (°)	30-60	45.00	39.57	60.00	53.10	30.00	30.00	30.00
Objective	$T_{max}(^{\circ}C)$	Minimization	35.96	34.98	38.93	35.02	36.49	35.86	35.47
functions	$P_{\mathbf{w}}(\mathbf{mW})$	Minimization	0.68	2.111	0.213	1.953	0.534	0.604	0.827
	$T_{\sigma}(K)$	Minimization	1.034	0.918	1.499	0.891	1.022	0.973	0.937
	M _{CP} (g)	Minimization	54.12	49.48	55.87	49.48	41.79	44.76	46.33

validated comprehensively against previous relevant numerical and experimental studies. This paper is novel in two key aspects. It is the first to develop and apply a novel ML-enabled multi-objective optimization (MOO) approach based on TOPSIS approaches for the thermal management of SMCCP-IVSMC cold plate configurations. Secondly, it is the first to reduce the cold plate mass in addition to the other thermohydraulic performance indicators, including the maximum temperature, water pumping power and temperature variations over the cold plate.

A sensitivity analysis carried out to identify the most critical design parameters, that have the biggest impact on the practical performance objectives, revealed that the width of the minichannels has the largest impact on the battery maximum temperature, battery temperature standard deviation, water pumping power, and the mass of the cold plate, with the width of the V-shaped minichannels and the V-shape intersecting angle being the next most influential parameters. Accurate surrogate models of the maximum battery temperature and battery temperature standard deviation, which determine battery longevity and safety, and the water pumping power and the mass of the cold plate materials, which affect the operating and manufacturing costs, respectively, can be constructed by combining Optimal Latin Hypercube sampling with Gaussian Process Regression surrogate modeling. These can be combined within a generalized differential evolution (GDE3) algorithm and TOPSIS approaches to create a powerful multi-objective optimisation methodology to enable designers to explore the available compromises between the various objectives.

A series of Pareto curves and surfaces are presented which demonstrate vividly that there are many significant opportunities for

optimizing the design of Li-ion cold plates by careful optimisation of the geometry of secondary channels. The optimisation results have identified a number of options for improving performance significantly, based on designers' preferences, beyond the current benchmark design. In addition to relatively modest reductions in the maximum temperature of 1 °C, operating costs can be minimised by reducing water pumping power by over 68.7 %, and material costs minimised by reducing the mass of the cold plate heat exchangers by over 22.8 %. Reductions in mass will also contribute to reducing energy consumption and improved acceleration performance and reduced braking distances. The topranked BCS using equally weighted TOPSIS has also been identified, which enables all four objectives to be reduced simultaneously. More generally, it is shown that the objectives are highly inter-dependent and any practical design will involve compromises between the objectives. The methodology developed here is a powerful new tool for enabling designers to meet their design objectives.

Future work could proceed in three fruitful directions. The first would be to carry out experimental investigations of the cold plate configurations examined here to provide further useful benchmark data for numerical validation. The second would be to analyse battery degradation and aging to assess how the optimised BTMS configuration in this study impacts long-term battery health, using the methodologies adopted by References [126,127]. The final future research direction would be to assess the impact of using other BTMS technologies, such as PCMs and hybrid cooling systems, and compare the overall efficiency and weight of these cooling systems with the performances achieved here.

CRediT authorship contribution statement

Ahmed Mahmood: Writing – original draft, Visualization, Validation, Software, Resources, Methodology, Investigation, Formal analysis, Data curation, Conceptualization. Gregory de Boer: Writing – review & editing, Supervision, Project administration. Timothy Cockerill: Writing – review & editing, Supervision, Project administration. Muhammad F.B. Raihan: Writing – review & editing, Visualization, Investigation. Harvey Thompson: Writing – review & editing, Supervision, Project administration, Funding acquisition, Conceptualization. Jochen Voss: Writing – review & editing, Supervision, Project administration.

Declaration of competing interest

The authors declare that they have no known competing financial

Appendix A

interests or personal relationships that could have appeared to influence the work reported in this paper.

Data availability

Data will be made available on request.

Acknowledgements

The author (Mr. Ahmed Mahmood) would like to thank the Higher Committee for Education Development (HCED) in Iraq for PhD sponsorship supports.

Table A.1
BCSs and closeness coefficients for four-objective optimisation using the general TOPSI method with equally weighted objectives, each with a weight of 0.25.

Design variables			BCS						
W _{ch} (mm)	$W_{int}(\boldsymbol{mm})$	0 (°)	$T_{max}(^{\circ}C)$	Τ _σ (K)	$P_{w}\left(mW\right)$	M _{CP} (g)			
5.00	3.46	30.00	35.86	0.973	0.6038	44.76	0.837		
5.00	3.09	30.00	35.68	0.956	0.6720	45.46	0.836		
5.00	3.63	30.00	35.95	0.981	0.5859	44.43	0.834		
5.00	2.64	30.00	35.47	0.937	0.8270	46.33	0.819		
5.00	3.92	51.35	36.30	0.990	0.5712	43.87	0.810		
5.00	2.73	39.57	35.78	0.953	0.7767	46.14	0.80		
5.00	4.82	52.41	36.42	1.006	0.5407	42.13	0.80		
4.89	3.70	36.63	36.23	0.995	0.5766	44.68	0.80		
5.00	5.00	30.00	36.49	1.022	0.5347	41.79	0.799		
4.92	2.29	30.00	35.34	0.930	1.0127	47.31	0.786		
5.00	1.96	53.10	35.50	0.924	0.9940	47.63	0.778		
4.33	4.28	59.55	36.68	1.051	0.4789	45.25	0.75		
4.33	3.80	59.55	36.59	1.041	0.4887	46.34	0.749		
5.00	1.64	43.61	35.28	0.917	1.2954	48.24	0.74		
3.90	4.68	51.36	36.87	1.093	0.4216	45.63	0.72		
4.99	1.64	30.00	35.13	0.913	1.6450	48.28	0.703		
4.89	1.30	51.36	35.21	0.908	1.5298	49.41	0.70		
3.30	4.09	32.24	36.94	1.128	0.4175	49.11	0.663		
3.30	4.48	32.24	37.11	1.142	0.3937	48.01	0.66		
5.00	1.00	53.10	35.02	0.891	1.9531	49.48	0.66		
5.00	1.00	39.57	34.98	0.918	2.1111	49.48	0.64		
4.99	1.30	30.00	35.07	0.913	2.1936	48.93	0.63		
3.17	3.65	49.90	37.17	1.157	0.3743	50.82	0.61		
5.00	1.19	30.00	35.06	0.914	2.4009	49.12	0.61		
2.90	5.00	36.64	37.55	1.214	0.3390	47.72	0.61		
5.00	1.14	30.00	35.05	0.915	2.4928	49.21	0.60		
2.97	4.98	59.19	37.77	1.245	0.3186	47.57	0.59		
3.11	3.58	59.81	37.41	1.182	0.3477	51.24	0.593		
5.00	1.04	30.00	35.05	0.916	2.6981	49.40	0.586		
5.00	1.01	30.00	35.05	0.917	2.7669	49.46	0.579		
2.97	3.58	59.81	37.57	1.211	0.3301	51.77	0.569		
2.91	2.24	48.39	36.76	1.142	0.4675	56.07	0.568		
2.60	3.58	46.79	37.71	1.266	0.3180	53.17	0.529		
2.35	4.91	30.00	38.17	1.351	0.2756	49.67	0.52		
2.60	3.32	60.00	37.95	1.295	0.2912	53.99	0.50		
2.38	5.00	60.00	38.63	1.427	0.2623	49.28	0.486		
2.34	3.58	46.79	38.06	1.333	0.2891	54.13	0.48		
2.37	4.32	59.28	38.51	1.390	0.2735	51.58	0.47		
2.37	3.35	60.00	38.29	1.366	0.2600	54.81	0.46		
2.26	3.28	60.00	38.42	1.396	0.2491	55.47	0.44		
2.00	4.47	50.94	38.91	1.470	0.2442	52.31	0.440		
2.00	5.00	58.92	39.10	1.528	0.2364	50.45	0.44		
2.20	1.96	59.78	37.83	1.344	0.3153	60.24	0.43		
2.00	5.00	60.00	39.24	1.564	0.2315	50.45	0.430		
2.00	4.97	60.00	39.24	1.563	0.2329	50.57	0.42		
2.13	3.57	59.79	38.72	1.450	0.2310	54.97	0.429		

(continued on next page)

Table A.1 (continued)

Design variables			BCS					
$\overline{W_{ch}(mm)}$	$W_{ch}(mm)$ $W_{int}(mm)$ $\Theta(^{\circ})$		$T_{max}(^{\circ}C)$	Τ _σ (K)	$P_{w}\left(mW\right)$	M _{CP} (g)		
2.00	4.00	59.69	39.07	1.516	0.2298	53.97	0.4144	
2.00	3.46	60.00	38.93	1.499	0.2134	55.87	0.4079	
2.00	3.08	60.00	38.77	1.479	0.2219	57.21	0.4056	
2.00	2.86	60.00	38.67	1.467	0.2323	57.98	0.4046	

Table A.2 BCSs, and closeness coefficients for four-objective optimization using the entropy-weighted TOPSIS method, with objective weights of 0.381 for T_{max} , 0.314 for T_{σ} , 0.156 for P_{w} , and 0.149 for M_{CP} .

Design variables			BCS						
$\overline{W_{ch}(mm)}$	$W_{int}(mm)$	0 (°)	$T_{max}(^{\circ}C)$	Τ _σ (K)	$P_w(mW)$	M _{CP} (g)			
5.00	2.64	30.00	35.47	0.937	0.8270	46.33	0.8688		
4.92	2.29	30.00	35.34	0.930	1.0127	47.31	0.8641		
5.00	3.09	30.00	35.68	0.956	0.6720	45.46	0.8510		
5.00	1.96	53.10	35.50	0.924	0.9940	47.63	0.8502		
5.00	1.64	43.61	35.28	0.917	1.2954	48.24	0.8443		
5.00	2.73	39.57	35.78	0.953	0.7767	46.14	0.8316		
5.00	3.46	30.00	35.86	0.973	0.6038	44.76	0.8269		
4.99	1.64	30.00	35.13	0.913	1.6450	48.28	0.8265		
4.89	1.30	51.36	35.21	0.908	1.5298	49.41	0.8247		
5.00	3.63	30.00	35.95	0.981	0.5859	44.43	0.8139		
5.00	1.00	53.10	35.02	0.891	1.9531	49.48	0.8030		
5.00	1.00	39.57	34.98	0.918	2.1111	49.48	0.7898		
4.99	1.30	30.00	35.07	0.913	2.1936	48.93	0.7851		
5.00	1.19	30.00	35.06	0.914	2.4009	49.12	0.7702		
4.89	3.70	36.63	36.23	0.995	0.5766	44.68	0.7699		
5.00	3.92	51.35	36.30	0.990	0.5712	43.87	0.7641		
5.00	1.14	30.00	35.05	0.915	2.4928	49.21	0.7636		
5.00	1.04	30.00	35.05	0.916	2.6981	49.40	0.7491		
5.00	4.82	52.41	36.42	1.006	0.5407	42.13	0.7465		
5.00	1.01	30.00	35.05	0.917	2.7669	49.46	0.7443		
5.00	5.00	30.00	36.49	1.022	0.5347	41.79	0.7317		
4.33	3.80	59.55	36.59	1.041	0.4887	46.34	0.7006		
4.33	4.28	59.55	36.68	1.051	0.4789	45.25	0.6872		
3.90	4.68	51.36	36.87	1.093	0.4216	45.63	0.6453		
3.30	4.09	32.24	36.94	1.128	0.4175	49.11	0.6080		
2.91	2.24	48.39	36.76	1.142	0.4675	56.07	0.5899		
3.30	4.48	32.24	37.11	1.142	0.3937	48.01	0.5867		
3.17	3.65	49.90	37.17	1.157	0.3743	50.82	0.5626		
3.11	3.58	59.81	37.41	1.182	0.3477	51.24	0.5225		
2.90	5.00	36.64	37.55	1.214	0.3390	47.72	0.5055		
2.97	3.58	59.81	37.57	1.211	0.3301	51.77	0.4906		
2.97	4.98	59.19	37.77	1.245	0.3186	47.57	0.4705		
2.60	3.58	46.79	37.71	1.266	0.3180	53.17	0.4456		
2.60	3.32	60.00	37.95	1.295	0.2912	53.99	0.4073		
2.35	4.91	30.00	38.17	1.351	0.2756	49.67	0.3804		
2.34	3.58	46.79	38.06	1.333	0.2891	54.13	0.3800		
2.20	1.96	59.78	37.83	1.344	0.3153	60.24	0.3785		
2.37	3.35	60.00	38.29	1.366	0.2600	54.81	0.3452		
2.37	4.32	59.28	38.51	1.390	0.2735	51.58	0.3304		
2.26	3.28	60.00	38.42	1.396	0.2491	55.47	0.3220		
2.38	5.00	60.00	38.63	1.427	0.2623	49.28	0.3200		
2.13	3.57	59.79	38.72	1.450	0.2310	54.97	0.2865		
2.00	4.47	50.94	38.91	1.470	0.2442	52.31	0.2793		
2.00	2.86	60.00	38.67	1.467	0.2323	57.98	0.2765		
2.00	3.08	60.00	38.77	1.479	0.2219	57.21	0.2697		
2.00	5.00	58.92	39.10	1.528	0.2364	50.45	0.2673		
2.00	3.46	60.00	38.93	1.499	0.2134	55.87	0.2611		
2.00	5.00	60.00	39.24	1.564	0.2315	50.45	0.2511		
2.00	4.97	60.00	39.24	1.563	0.2329	50.57	0.2578		
2.00	4.00	59.69	39.07	1.516	0.2298	53.97	0.2568		

References

- [1] D. Tuncer, E. Yilmaz Ulu, Contribution of regenerative suspension module to charge efficiency and range in hydrogen fuel cell electric vehicles, Int. J. Hydrog. Energy 75 (2024) 547–556, https://doi.org/10.1016/j.ijhydene.2024.03.219.
- [2] M.A. Bamdezh, G.R. Molaeimanesh, The effect of active and passive battery thermal management systems on energy consumption, battery degradation, and carbon emissions of an electric vehicle, Energy 304 (2024) 132134, https://doi. org/10.1016/j.energy.2024.132134.
- [3] S. Abdul Qadir, F. Ahmad, A. Mohsin A B Al-Wahedi, A. Iqbal, A. Ali, Navigating the complex realities of electric vehicle adoption: a comprehensive study of

- government strategies, policies, and incentives, Energy Strategy Rev. 53 (2024) 101379, https://doi.org/10.1016/j.esr.2024.101379.
- [4] Y. Lei, L. Xu, Q.N. Chan, A. Li, A.C. Yin Yuen, Y. Yuan, G.H. Yeoh, W. Wang, Recent advances in separator design for lithium metal batteries without dendrite formation: implications for electric vehicles, eTransportation 20 (2024) 100330, https://doi.org/10.1016/j.etran.2024.100330.
- [5] A. Hussain, C.Y. Tso, C.Y.H. Chao, Experimental investigation of a passive thermal management system for high-powered lithium ion batteries using nickel foam-paraffin composite, Energy 115 (2016) 209–218, https://doi.org/10.1016/ j.energy.2016.09.008.
- [6] A. Greco, X. Jiang, D. Cao, An investigation of lithium-ion battery thermal management using paraffin/porous-graphite-matrix composite, J. Power Sources 278 (2015) 50–68, https://doi.org/10.1016/j.jpowsour.2014.12.027.
- [7] M. Tousi, A. Sarchami, M. Kiani, M. Najafi, E. Houshfar, Numerical study of novel liquid-cooled thermal management system for cylindrical Li-ion battery packs under high discharge rate based on AgO nanofluid and copper sheath, J Energy Storage 41 (2021) 102910, https://doi.org/10.1016/j.est.2021.102910.
- [8] M. Hussain, M.K. Khan, M. Pathak, Thermal management of high-energy lithium titanate oxide batteries using an effective channeled dielectric fluid immersion cooling system, Energy Convers. Manag. 313 (2024) 118644, https://doi.org/ 10.1016/j.enconman.2024.118644.
- [9] A. Yadav, M. Samykano, A.K. Pandey, S.K. Natarajan, G. Vasudevan, G. Muthuvairavan, S.K. Suraparaju, Sustainable phase change material developments for thermally comfortable smart buildings: a critical Review, Process. Saf. Environ. Prot. (2024), https://doi.org/10.1016/j.psep.2024.09.025.
- [10] F. Cao, Z. Li, Y. Zhang, X. Wang, L. Zhu, S. Zhang, B. Tang, Silica-based aerogels encapsulate organic/inorganic composite phase change materials for building thermal management, J Energy Storage 97 (2024) 112858, https://doi.org/ 10.1016/j.est.2024.112858.
- [11] C. Tan, M. Zhang, J. Yang, X. Wang, W. Zhao, J. Li, Q. Zhao, X. Tian, Ultra-high performance Cu-Al-Ni as phase change material for thermal management of highpower electronic devices, J Energy Storage 113 (2025) 115635, https://doi.org/ 10.1016/j.est.2025.115635.
- [12] M.E. Demir, H.S. Erden, Effective energy use and passive cooling in data centers using heat pipes and PCM-integrated TEG systems, J Energy Storage 122 (2025) 116625, https://doi.org/10.1016/j.est.2025.116625.
- [13] C. Liu, N. Hao, T. Zhang, D. Wang, Z. Li, W. Bian, Optimization of data-center immersion cooling using liquid air energy storage, J Energy Storage 90 (2024) 111806, https://doi.org/10.1016/j.est.2024.111806.
- [14] A. Sharma, M. Khatamifar, W. Lin, R. Pitchumani, A state-of-the-art review on numerical investigations of liquid-cooled battery thermal management systems for lithium-ion batteries of electric vehicles, J Energy Storage 101 (2024) 113844, https://doi.org/10.1016/j.est.2024.113844.
- [15] E.B. Agyekum, F. Odoi-Yorke, S. Mirzaliev, M. Abdullah, F.L. Rashid, A. K. Hussein, Review of trends and emerging optimization techniques for battery thermal management traditional and bibliometric approach, J Energy Storage 119 (2025) 116437, https://doi.org/10.1016/j.est.2025.116437.
- [16] S. Kharabati, S. Saedodin, A systematic review of thermal management techniques for electric vehicle batteries, J Energy Storage 75 (2024) 109586, https://doi.org/10.1016/j.est.2023.109586.
- [17] C. Xie, X. Yang, Heat transfer enhancement of microchannel using nanoencapsulated phase change material for fuel cell thermal management systems, J Energy Storage 103 (2024) 114370, https://doi.org/10.1016/j. est.2024.114370.
- [18] J. Hosseinpour, O.B. Rizvandi, R.J. Braun, Enhancing thermal management in a reversible solid oxide cell system utilizing thermal energy storage, J Energy Storage 114 (2025) 115806, https://doi.org/10.1016/j.est.2025.115806.
 [19] H. Dirawi, Q. Wang, M. Hu, Y. Su, S. Riffat, A hydronic closed-loop photovoltaic
- [19] H. Dirawi, Q. Wang, M. Hu, Y. Su, S. Riffat, A hydronic closed-loop photovoltaic cooling system designed for hot and arid regions: performance evaluation and degradation rate/lifetime analysis, Appl. Energy 373 (2024) 123999, https://doi. org/10.1016/j.apenergy.2024.123999.
- [20] H. Dirawi, Q. Wang, M. Hu, Y. Su, S. Riffat, Comprehensive performance analysis of a novel closed-loop hydronic cooling of photovoltaic panel with a controlled intermittent flow strategy, Renew. Energy 239 (2025) 122185, https://doi.org/ 10.1016/j.renene.2024.122185.
- [21] M.A. Alnakeeb, M.A. Abdel Salam, M.A. Hassab, W.M. El-Maghlany, Numerical study of thermal and electrical performance of a new configuration of hybrid photovoltaic solar panel phase-change material cooling system, J Energy Storage 97 (2024) 112945, https://doi.org/10.1016/j.est.2024.112945.
- [22] G. Nobrega, B. Cardoso, R. Souza, J. Pereira, P. Pontes, S.O. Catarino, D. Pinho, R. Lima, A. Moita, A review of novel heat transfer materials and fluids for aerospace applications, Aerospace 11 (2024), https://doi.org/10.3390/ aerospace11040275.
- [23] A. Mahmood, T. Cockerill, G. de Boer, J. Voss, H. Thompson, Heat transfer modeling and optimal thermal management of electric vehicle battery systems, Energies 17 (2024), https://doi.org/10.3390/en17184575.
- [24] G. Lu, M.-Y. Huang, Y. Liu, L. Wang, J.-J. Zhao, J.-H. Meng, Numerical investigation and parameter optimization on a novel self-crossing flow channel liquid-cooled plate for battery thermal management, J Energy Storage 121 (2025) 116586, https://doi.org/10.1016/j.est.2025.116586.
- [25] H. Hu, J. Xu, J. Li, H. Xi, Immersion coupled direct cooling with non-uniform cooling pipes for efficient lithium-ion battery thermal management, J Energy Storage 116 (2025) 116010, https://doi.org/10.1016/j.est.2025.116010.
- [26] F. Ren, Q. Li, P. Wang, Multi-objective optimization of tesla valve channel battery cold plate with nanofluid by RSM and NSGA-II, J Energy Storage 115 (2025) 115969, https://doi.org/10.1016/j.est.2025.115969.

- [27] S. Amosedinakaran, R. Kannan, S. Kannan, A. Ramkumar, S. Suresh, A. Bhuvanesh, Performance analysis for battery stability improvement using direct air cooling mechanism for electric vehicles, e-Prime - Adv. Electr. Eng. Electron. Energy 8 (2024) 100585, https://doi.org/10.1016/j. prime.2024.100585.
- [28] A. Sharma, N.K. Shukla, A. Garg, M.M. Alammar, R. Raman, D. Mukherjee, L. Li, Influence of uncertainties in a battery pack with air cooling for electric vehicles on temperature difference and volume of battery module, J Energy Storage 113 (2025) 115643, https://doi.org/10.1016/j.est.2025.115643.
- [29] H. Cho, H. Lee, S. Ryu, Sequential multi-objective Bayesian optimization of air-cooled battery thermal management system with spoiler integration, J Energy Storage 114 (2025) 115586, https://doi.org/10.1016/j.est.2025.115586.
- [30] M. Kumar, S.Y. Khan, S. Liu, A.A. Zaidi, Z. Shaoliang, A. Sohrabi, J. Rashidov, Scientific mapping and review of the research landscape in battery thermal management strategies using heat pipe, J Energy Storage 103 (2024) 114147, https://doi.org/10.1016/j.est.2024.114147.
- [31] A.M. Fathoni, N. Putra, T.M.I. Mahlia, A systematic review of battery thermal management systems based on heat pipes, J Energy Storage 73 (2023) 109081, https://doi.org/10.1016/j.est.2023.109081.
- [32] A.M. Fathimathul Faseena, A. Sreekumar, Advances, perspectives and challenges in phase change material based battery thermal management: a comprehensive review, J Energy Storage 113 (2025) 115644, https://doi.org/10.1016/j. est 2025 115644
- [33] L. Jie, J. Zhang, Y. Fan, Z. Yu, W. Pan, A review of composite phase change materials used in battery thermal management systems, J Energy Storage 112 (2025) 115579, https://doi.org/10.1016/j.est.2025.115579.
- [34] M. Nasiri, H. Hadim, Thermal management of Li-ion batteries using phase change materials: recent advances and future challenges, J Energy Storage 111 (2025) 115440, https://doi.org/10.1016/j.est.2025.115440.
- [35] R.K. Pal, J.K.S. Paw, P. Ganesan, C.W. Tong, Modeling and simulation of phase change material-based passive and hybrid thermal management systems for lithium-ion batteries: a comprehensive review, J Energy Storage 116 (2025) 116011, https://doi.org/10.1016/j.est.2025.116011.
- [36] X. Zhang, S. Wu, C. Zhang, Improving thermal performance of micro heat pipe arrays by integration of phase change material, J Energy Storage 118 (2025) 116301, https://doi.org/10.1016/j.est.2025.116301.
- [37] Z. Tang, P. Yu, M. Li, C. Tao, J. Cheng, Thermal management characteristics of a novel cylindrical lithium-ion battery module using liquid cooling, phase change materials, and heat pipes, J Energy Storage 99 (2024) 113350, https://doi.org/ 10.1016/j.est.2024.113350.
- [38] R. Bao, Z. Wang, H. Yang, B. Zhang, Q. Gao, S. Chen, Comparison analysis of thermal behavior of Lithium-ion batteries based on a novel multi-modal composite immersion liquid cooling system coupled with fin/micro-heat pipe array, J Energy Storage 104 (2024) 114379, https://doi.org/10.1016/j. cot/2004.114779
- [39] M.S. P. T, D.K. Bal, B.B. Sahoo, A technical review on controlling the Li-ion battery temperature through composite phase change materials and hybrid cooling techniques, J. Energy Storage 112 (2025) 115584, https://doi.org/ 10.1016/j.est.2025.115584.
- [40] S. Koundal, S.L. Sharma, A. Debbarma, Battery thermal management systems for electric vehicles: an overview of cooling techniques and performance optimization, J. Therm. Anal. Calorim. 150 (2025) 5855–5882, https://doi.org/ 10.1007/s10973-025-14170-3
- [41] P. Paneerselvam, N. SK, V. Suyamburajan, T. Murugaiyan, K. Singh Shekhawat, G. Rengasamy, A review on recent progress in battery thermal management system in electric vehicle application, Mater. Today Proc. (2024), https://doi. org/10.1016/j.matpr.2024.04.094.
- [42] H. Liu, S. Ahmad, Y. Shi, J. Zhao, A parametric study of a hybrid battery thermal management system that couples PCM/copper foam composite with helical liquid channel cooling, Energy 231 (2021) 120869, https://doi.org/10.1016/j. energy.2021.120869.
- [43] J. Kim, J. Oh, H. Lee, Review on battery thermal management system for electric vehicles, Appl. Therm. Eng. 149 (2019) 192–212, https://doi.org/10.1016/j. applthermaleng.2018.12.020.
- [44] S.S. Katoch, M. Eswaramoorthy, A detailed review on electric vehicles battery thermal management system, IOP Conf. Ser.: Mater. Sci. Eng. 912 (2020) 042005, https://doi.org/10.1088/1757-899X/912/4/042005.
- [45] A. Bhosale, V. Deshmukh, M. Chaudhari, A comprehensive assessment of emerging trends in battery thermal management systems, J. Braz. Soc. Mech. Sci. Eng. 46 (2024) 145, https://doi.org/10.1007/s40430-024-04735-y.
- [46] G. Murali, G.S.N. Sravya, J. Jaya, V. Naga Vamsi, A review on hybrid thermal management of battery packs and it's cooling performance by enhanced PCM, Renew. Sust. Energ. Rev. 150 (2021) 111513, https://doi.org/10.1016/j. rser.2021.111513.
- [47] C. Wu, J. Ni, X. Shi, R. Huang, A new design of cooling plate for liquid-cooled battery thermal management system with variable heat transfer path, Appl. Therm. Eng. 239 (2024) 122107, https://doi.org/10.1016/j. applthermaleng.2023.122107.
- [48] X. Du, Z. Wang, Q. Gao, H. Yang, R. Bao, S. Xiong, Study on novel battery thermal management using triply periodic minimal surface porous structures liquid cooling channel, Appl. Therm. Eng. 257 (2024) 124384, https://doi.org/ 10.1016/j.applthermaleng.2024.124384.
- [49] C. Wu, X. Yuan, B. Kong, Y. Zou, H. Shi, Innovative liquid cooling channel enhanced battery thermal management (BTM) structure based on stepwise optimization method, J Energy Storage 81 (2024) 110485, https://doi.org/ 10.1016/j.est.2024.110485.

- [50] J. Zhu, J. Wang, D. Cheng, J. Mao, K. Zhang, Numerical investigation and parameter optimization on a rib-grooved liquid-cooled plate for lithium battery thermal management system, J Energy Storage 85 (2024) 111085, https://doi. org/10.1016/j.est.2024.111085.
- [51] Z. Sui, H. Lin, Q. Sun, K. Dong, W. Wu, Multi-objective optimization of efficient liquid cooling-based battery thermal management system using hybrid manifold channels, Appl. Energy 371 (2024) 123766, https://doi.org/10.1016/j. appergy.2024.123766.
- [52] M. Nasiri, H. Hadim, Advances in battery thermal management: Current landscape and future directions, Renew. Sust. Energ. Rev. 200 (2024) 114611, https://doi.org/10.1016/j.rser.2024.114611.
- [53] Q.L. Yue, C.X. He, M.C. Wu, T.S. Zhao, Advances in thermal management systems for next-generation power batteries, Int. J. Heat Mass Transf. 181 (2021) 121853, https://doi.org/10.1016/j.ijheatmasstransfer.2021.121853.
- [54] F.S. Hwang, T. Confrey, C. Reidy, D. Picovici, D. Callaghan, D. Culliton, C. Nolan, Review of battery thermal management systems in electric vehicles, Renew. Sust. Energ. Rev. 192 (2024) 114171, https://doi.org/10.1016/j.rser.2023.114171.
- [55] B.B. Kanbur, Y. Zhou, M.H. Seat, W.B. Markussen, M.R. Kærn, F. Duan, Experimental study on indirect liquid cooling performance of metal 3D-printed cold plates for battery thermal management, Heat Transfer Eng. 45 (2024) 1412–1430, https://doi.org/10.1080/01457632.2023.2260525.
- [56] K. Monika, C. Chakraborty, S. Roy, S. Dinda, S.A. Singh, S.P. Datta, Parametric investigation to optimize the thermal management of pouch type lithium-ion batteries with mini-channel cold plates, Int. J. Heat Mass Transf. 164 (2021) 120568, https://doi.org/10.1016/j.ijheatmasstransfer.2020.120568.
- [57] Y. Li, Z. Zhou, W.-T. Wu, Three-dimensional thermal modeling of Li-ion battery cell and 50 V Li-ion battery pack cooled by mini-channel cold plate, Appl. Therm. Eng. 147 (2019) 829–840, https://doi.org/10.1016/j. applthermaleng.2018.11.009.
- [58] M.S. Patil, J.-H. Seo, S. Panchal, S.-W. Jee, M.-Y. Lee, Investigation on thermal performance of water-cooled Li-ion pouch cell and pack at high discharge rate with U-turn type microchannel cold plate, Int. J. Heat Mass Transf. 155 (2020) 119728, https://doi.org/10.1016/j.ijheatmasstransfer.2020.119728.
- [59] J. Pu, X.-F. Ping, S. Panchal, N. Hua, D.R. Fraser, D.M. Fowler, X.K. Zhang, Structural Optimization of a Serpentine-Channel Cold Plate for Thermal Management of Lithium-Ion Battery Based on the Field Synergy Principle, Available at SSRN 4795285, 2024.
- [60] H. Dai, W. Tian, M. Hou, S. Liu, C. Zhang, Z. Wei, Z. Dong, C.S. Chin, Enhancing thermal management in electric commercial vehicles: a novel liquid-cooled multiple parallel-serpentine channels, J Energy Storage 107 (2025) 114708, https://doi.org/10.1016/j.est.2024.114708.
- [61] K. Monika, C. Chakraborty, S. Roy, S. Dinda, S.A. Singh, S.P. Datta, Selection of an ideal coolant to ward off the thermal runaway of a pouch type Li-ion battery module, J. Electrochem. Energy Convers. Storage 18 (2021), https://doi.org/ 10.1115/1.4049568.
- [62] X. Fan, C. Meng, Y. Yang, J. Lin, W. Li, Y. Zhao, S. Xie, C. Jiang, Numerical optimization of the cooling effect of a bionic fishbone channel liquid cooling plate for a large prismatic lithium-ion battery pack with high discharge rate, J Energy Storage 72 (2023) 108239, https://doi.org/10.1016/j.est.2023.108239.
 [63] D. Zhao, Z. Lei, C. An, Research on battery thermal management system based on
- [63] D. Zhao, Z. Lei, C. An, Research on battery thermal management system based or liquid cooling plate with honeycomb-like flow channel, Appl. Therm. Eng. 218 (2023) 119324, https://doi.org/10.1016/j.applthermaleng.2022.119324.
- [64] Y. Wang, X. Xu, Z. Liu, J. Kong, Q. Zhai, H. Zakaria, Q. Wang, F. Zhou, H. Wei, Optimization of liquid cooling for prismatic battery with novel cold plate based on butterfly-shaped channel, J Energy Storage 73 (2023) 109161, https://doi. org/10.1016/j.est.2023.109161.
- [65] L. Chen, D. Deng, Q. Ma, Y. Yao, X. Xu, Performance evaluation of high concentration photovoltaic cells cooled by microchannels heat sink with serpentine reentrant microchannels, Appl. Energy 309 (2022) 118478, https://doi.org/10.1016/j.apenergy.2021.118478.
- [66] K. Monika, S.P. Datta, Comparative assessment among several channel designs with constant volume for cooling of pouch-type battery module, Energ. Convers. Manage. 251 (2022) 114936, https://doi.org/10.1016/j.
- [67] N. Wang, C. Li, W. Li, X. Chen, Y. Li, D. Qi, Heat dissipation optimization for a serpentine liquid cooling battery thermal management system: an application of surrogate assisted approach, J Energy Storage 40 (2021) 102771, https://doi.org/ 10.1016/j.est.2021.102771.
- [68] M.Z. Saghir, M. Yahya, Cooling lithium-ion batteries in the presence of triply periodic minimal surfaces structure, Appl. Sol. Energy 60 (2024) 357–369, https://doi.org/10.3103/S0003701X24600139.
- [69] N. Kaewchoothong, C. Nuntadusit, S. Gonsrang, M. Luengchavanon, S. Chatpun, Numerical study on flow field and heat transfer enhancement in a cooling channel with novel ribs based on battery thermal management system, Heat Transf. Eng. (2024) 1–16, https://doi.org/10.1080/01457632.2024.2337977.
- [70] J.S. Sakkera, R. Chintalapudi, B. Pappula, S. Makgato, Novel design of serpentine channel heat sinks with rectangular and triangular ribs and grooves for 25Ah Liion battery thermal management, Int. J. Thermofluids (2024) 101011, https:// doi.org/10.1016/j.ijft.2024.101011.
- [71] H. Xu, S. Xiong, W. Li, L. Wu, Z. Wang, Heat transfer improvement of prismatic lithium-ion batteries via a mini-channel liquid-cooling plate with vortex generators, J. Electrochem. Energy Convers. Storage 21 (2023), https://doi.org/ 10.1115/1.4063324.
- [72] M.F.B. Raihan, Design Optimisation of Serpentine mini-Channel Heat Sink, University of Leeds, 2022.

- [73] A.F. Al-Neama, Z. Khatir, N. Kapur, J. Summers, H.M. Thompson, An experimental and numerical investigation of chevron fin structures in serpentine minichannel heat sinks, Int. J. Heat Mass Transf. 120 (2018) 1213–1228, https:// doi.org/10.1016/j.ijheatmasstransfer.2017.12.092.
- [74] L. Fan, J. Li, Y. Chen, D. Zhou, Z. Jiang, J. Sun, Study on the cooling performance of a new secondary flow serpentine liquid cooling plate used for lithium battery thermal management, Int. J. Heat Mass Transf. 218 (2024) 124711, https://doi. org/10.1016/j.ijheatmasstransfer.2023.124711.
- [75] H. Liu, X. Gao, D. Niu, M. Yu, Y. Ji, Thermal-hydraulic characteristics of the liquid-based battery thermal management system with intersected serpentine channels, Water 14 (2022) 3148, https://doi.org/10.3390/w14193148.
- [76] H. Liu, X. Gao, J. Zhao, M. Yu, D. Niu, Y. Ji, Liquid-based battery thermal management system performance improvement with intersected serpentine channels, Renew. Energy 199 (2022) 640–652, https://doi.org/10.1016/j. reneps 2022 09 026
- [77] P. Stabile, F. Ballo, G. Mastinu, M. Gobbi, An ultra-efficient lightweight electric vehicle—power demand analysis to enable lightweight construction, Energies 14 (2021), https://doi.org/10.3390/en14030766.
- [78] S. Shan, L. Li, Q. Xu, L. Ling, Y. Xie, H. Wang, K. Zheng, L. Zhang, S. Bei, Numerical investigation of a compact and lightweight thermal management system with axially mounted cooling tubes for cylindrical lithium-ion battery module, Energy 274 (2023) 127410, https://doi.org/10.1016/j. energy.2023.127410.
- [79] H. Dileep, P. Dhanalakota, P.S. Mahapatra, A. Pattamatta, Performance assessment of a novel localized cooling system for battery thermal management at high ambient conditions, Appl. Therm. Eng. 266 (2025) 125756, https://doi.org/ 10.1016/j.applthermaleng.2025.125756.
- [80] H. Zhou, W. Li, D. Gong, C. Xue, X. Guo, Z. Song, Thermal performance of a hybrid thermal management system that couples PCM with liquid cooling for cylindrical lithium-ion battery, Appl. Therm. Eng. 274 (2025) 126736, https:// doi.org/10.1016/j.applthermaleng.2025.126736.
- [81] M. Khoshvaght-Aliabadi, P. Ghodrati, Y.T. Kang, Developing a novel battery thermal management system utilizing supercritical CO2 as the cooling medium, Appl. Energy 381 (2025) 125207, https://doi.org/10.1016/j. apenergy.2024.125207.
- [82] L. Sheng, L. Su, H. Zhang, K. Li, Y. Fang, W. Ye, Y. Fang, Numerical investigation on a lithium ion battery thermal management utilizing a serpentine-channel liquid cooling plate exchanger, Int. J. Heat Mass Transf. 141 (2019) 658–668, https://doi.org/10.1016/j.ijheatmasstransfer.2019.07.033.
- [83] H. Ren, L. Jia, C. Dang, Z. Qi, An electrochemical-thermal coupling model for heat generation analysis of prismatic lithium battery, J Energy Storage 50 (2022) 104277, https://doi.org/10.1016/j.est.2022.104277.
- [84] M. Doyle, T.F. Fuller, J. Newman, Modeling of galvanostatic charge and discharge of the lithium/polymer/insertion cell, J. Electrochem. Soc. 140 (1993) 1526, https://doi.org/10.1149/1.2221597.
- [85] U.S. Kim, J. Yi, C.B. Shin, T. Han, S. Park, Modelling the thermal behaviour of a lithium-ion battery during charge, J. Power Sources 196 (2011) 5115–5121, https://doi.org/10.1016/j.jpowsour.2011.01.103.
- [86] K.H. Kwon, C.B. Shin, T.H. Kang, C.-S. Kim, A two-dimensional modeling of a lithium-polymer battery, J. Power Sources 163 (2006) 151–157, https://doi.org/ 10.1016/j.jpowsour.2006.03.012.
- [87] Y. Gan, J. Wang, J. Liang, Z. Huang, M. Hu, Development of thermal equivalent circuit model of heat pipe-based thermal management system for a battery module with cylindrical cells, Appl. Therm. Eng. 164 (2020) 114523, https://doi. org/10.1016/j.applthermaleng.2019.114523.
- [88] G. Hou, X. Liu, W. He, C. Wang, J. Zhang, X. Zeng, Z. Li, D. Shao, An equivalent circuit model for battery thermal management system using phase change material and liquid cooling coupling, J Energy Storage 55 (2022) 105834, https://doi.org/10.1016/j.est.2022.105834.
- [89] Z. Gao, C.S. Chin, W.L. Woo, J. Jia, Integrated equivalent circuit and thermal model for simulation of temperature-dependent *LiFePO4* battery in actual embedded application, Energies 10 (2017), https://doi.org/10.3390/ en10010085.
- [90] J. Liu, S. Yadav, M. Salman, S. Chavan, S.C. Kim, Review of thermal coupled battery models and parameter identification for lithium-ion battery heat generation in EV battery thermal management system, Int. J. Heat Mass Transf. 218 (2024) 124748, https://doi.org/10.1016/j.ijheatmasstransfer.2023.124748.
- [91] V.-T. Ho, K. Chang, S.W. Lee, S.H. Kim, Transient thermal analysis of a Li-ion battery module for electric cars based on various cooling fan arrangements, in: Energies 13 (2020), https://doi.org/10.3390/en13092387.
- [92] N. Sophy-Mahfoudi, S.-V. Sekharam, M.h. Boutaous, S. Xin, Model-based design of LFP battery thermal management system for EV application, Batteries 10 (2024), https://doi.org/10.3390/batteries10090329.
- [93] P. Ashkboos, A. Yousefi, E. Houshfar, Design improvement of thermal management for Li-ion battery energy storage systems, Sustain Energy Technol Assess 44 (2021) 101094, https://doi.org/10.1016/j.seta.2021.101094.
- [94] S. Ahmad, Y. Liu, S.A. Khan, S.W.A. Shah, X. Huang, Modeling liquid immersion-cooling battery thermal management system and optimization via machine learning, Int. Commun. Heat Mass Transf. 158 (2024) 107835, https://doi.org/10.1016/j.icheatmasstransfer.2024.107835.
- [95] L. Wang, H. Zuo, B. Zhang, G. Jia, Effects of the cold plate with airfoil fins on the cooling performance enhancement of the prismatic LiFePO4 battery pack, Energy 296 (2024) 131210, https://doi.org/10.1016/j.energy.2024.131210.
- [96] L. Wang, H. Zuo, B. Zhang, G. Jia, Effects of supercritical carbon dioxide cooling on heat dissipation performance enhancement of a prismatic LiFePO4 battery

- pack, Energy 314 (2025) 134187, https://doi.org/10.1016/j.
- [97] H. Liu, H. Li, Y. Shi, Y. Ji, Performance evaluation of a novel cold plate with double-layer interdigitated flow channels for battery thermal management, Heat Transf. Eng. 46 (2024) 1750–1764, https://doi.org/10.1080/ 01457632.2024.2400865.
- [98] M. Panahi, H.R. Heydari, G. Karimi, Effects of micro heat pipe arrays on thermal management performance enhancement of cylindrical lithium-ion battery cells, Int. J. Energy Res. 45 (2021) 11245–11257, https://doi.org/10.1002/er.6604.
- [99] S. Zhan, Z. Cheng, Y. Yin, C. Yu, C. Zhao, Effect of inlet and outlet positions on heat dissipation performance of lithium-ion battery cold plates: an analysis based on topology optimization, Int. J. Heat Mass Transf. 215 (2023) 124436, https:// doi.org/10.1016/j.ijheatmasstransfer.2023.124436.
- [100] M. Leng, K. Liu, Y. Gao, H. Chen, P. Yan, X. Liu, Investigation of the electrical and thermal characteristics of soft-pack semi-solid-state lithium-ion batteries under high-rate discharge, J Energy Storage 97 (2024) 112682, https://doi.org/ 10.1016/j.est.2024.112682.
- [101] M. Akbarzadeh, J. Jaguemont, T. Kalogiannis, D. Karimi, J. He, L. Jin, P. Xie, J. Van Mierlo, M. Berecibar, A novel liquid cooling plate concept for thermal management of lithium-ion batteries in electric vehicles, Energy Convers. Manag. 231 (2021) 113862, https://doi.org/10.1016/j.enconman.2021.113862.
- [102] H. Liu, Z. Wei, W. He, J. Zhao, Thermal issues about Li-ion batteries and recent progress in battery thermal management systems: a review, Energ. Convers. Manage. 150 (2017) 304–330, https://doi.org/10.1016/j. enconman.2017.08.016.
- [103] A. Al-Waaly, The Effect of Heat Transfer on Temperature Measurement and It's Applications to Study Microchannel Heat Sinks PhD, University of Glasgow, 2015.
- [104] X. Chen, L. Jie, P. Yufei, C. Jie, C. Lihua, C. Gong, Developing a new mesh quality evaluation method based on convolutional neural network, Eng. Appl. Comput. Fluid Mech. 14 (2020) 391–400, https://doi.org/10.1080/ 13942660.2020.1720820
- [105] A. Tikadar, T.C. Paul, S.K. Oudah, N.M. Abdulrazzaq, A.S. Salman, J.A. Khan, Enhancing thermal-hydraulic performance of counter flow mini-channel heat sinks utilizing secondary flow: numerical study with experimental validation, Int. Commun. Heat Mass Transf. 111 (2020) 104447, https://doi.org/10.1016/j. icheatmasstransfer.2019.104447.
- [106] S. Chen, X. Peng, N. Bao, A. Garg, A comprehensive analysis and optimization process for an integrated liquid cooling plate for a prismatic lithium-ion battery module, Appl. Therm. Eng. 156 (2019) 324–339, https://doi.org/10.1016/j. applthermaleng.2019.04.089.
- [107] F. Zhang, X. Lu, L. Zhang, K. Xiao, F. Lu, Y. He, Y. Zhu, H. Gou, Bionic liquid cooling plate thermal management system based on flow resistance-thermal resistance model, Int. J. Therm. Sci. 190 (2023) 108336, https://doi.org/ 10.1016/j.ijthermalsci.2023.108336.
- [108] Z. Zhu, X. Wu, H. Zhang, Y. Guo, G. Wu, Multi-objective optimization of a liquid cooled battery module with collaborative heat dissipation in both axial and radial directions, Int. J. Heat Mass Transf. 155 (2020) 119701, https://doi.org/ 10.1016/j.iiheatmasstransfer 2020 119701
- [109] X. Wu, Z. Zhu, H. Zhang, S. Xu, Y. Fang, Z. Yan, Structural optimization of light-weight battery module based on hybrid liquid cooling with high latent heat PCM, Int. J. Heat Mass Transf. 163 (2020) 120495, https://doi.org/10.1016/j.iiheatmasstransfer.2020.120495.
- [110] L. Jin, H. Xi, Multi-objective parameter optimization of the Z-type air-cooling system based on artificial neural network, J Energy Storage 86 (2024) 111284, https://doi.org/10.1016/j.est.2024.111284.
- [111] B. Kavasoğullari, M.E. Karagöz, A.S. Yildiz, E. Biçer, Numerical investigation of the performance of a hybrid battery thermal management system at high discharge rates, J Energy Storage 73 (2023) 108982, https://doi.org/10.1016/j. est.2023.108982.

- [112] Q. Jiang, Y. Zhang, Y. Liu, R. Xu, J. Zhu, J. Wang, Structural optimization of serpentine channel water-cooled plate for lithium-ion battery modules based on multi-objective Bayesian optimization algorithm, J Energy Storage 91 (2024) 112136, https://doi.org/10.1016/j.est.2024.112136.
- [113] Y. Liu, X. Wang, L. Wang, Interval uncertainty analysis for static response of structures using radial basis functions, Appl. Math. Model. 69 (2019) 425–440, https://doi.org/10.1016/j.apm.2018.12.018.
- [114] Y. Nie, Y. Du, Z. Xu, Z. Zhang, Y. Qi, RBF interpolation algorithm for FTS tool path generation, Math. Probl. Eng. 2021 (2021) 6689200, https://doi.org/10.1155/ 2021/6689200.
- [115] H.S. Hamad, N. Kapur, Z. Khatir, O.M. Querin, H.M. Thompson, Y. Wang, M.C. T. Wilson, Computational fluid dynamics analysis and optimisation of polymerase chain reaction thermal flow systems, Appl. Therm. Eng. 183 (2021) 116122, https://doi.org/10.1016/j.applthermaleng.2020.116122.
- [116] I. Salahshoori, A. Yazdanbakhsh, A. Baghban, Machine learning-powered estimation of malachite green photocatalytic degradation with NML-BiFeO3 composites, Sci. Rep. 14 (2024) 8676, https://doi.org/10.1038/s41598-024-58076.x
- [117] J.R.R.A. Martins, A. Ning, Engineering Design Optimization, Cambridge University Press, Cambridge, 2021.
- [118] M.B. Bicer, E. Avsar Aydin, Analyzing equilateral triangle compact microstrip antennas using Gaussian process regression for telemedicine and mobile biomedical imaging systems, Multimed. Tools Appl. 83 (2024) 24435–24465, https://doi.org/10.1007/s11042-023-16470-y.
- [119] A. Singh, N. Nawayseh, H. Singh, Y.K. Dhabi, S. Samuel, Internet of agriculture: analyzing and predicting tractor ride comfort through supervised machine learning, Eng. Appl. Artif. Intell. 125 (2023) 106720, https://doi.org/10.1016/j. engappai.2023.106720.
- [120] D. Duvenaud, Automatic Model Construction With Gaussian Processes vol. Ph, University of Cambridge, UK, 2014, https://doi.org/10.17863/CAM.14087. D. Thesis..
- [121] B. Leite, A.O.S.d. Costa, E.F.d. Costa Junior, Multi-objective optimization of adiabatic styrene reactors using Generalized Differential Evolution 3 (GDE3), Chem. Eng. Sci. 265 (2023) 118196, https://doi.org/10.1016/j.ces.2022.118196.
- [122] S. Kukkonen, J. Lampinen, GDE3: the third evolution step of generalized differential evolution, in: 2005 IEEE Congress on Evolutionary Computation, Vol. 1, Edinburgh, UK Vol. 441, 2005, pp. 443–450, https://doi.org/10.1109/ CEC.2005.1554717.
- [123] M.R. Zare Banadkouki, Selection of strategies to improve energy efficiency in industry: a hybrid approach using entropy weight method and fuzzy TOPSIS, Energy 279 (2023) 128070, https://doi.org/10.1016/j.energy.2023.128070.
- [124] H. Lahmar, M. Dahane, K.N. Mouss, M. Haoues, Multi-objective sustainable production planning for a hybrid multi-stage manufacturing-remanufacturing system with grade-based classification of recovered and remanufactured products, J. Intell. Manuf. 36 (2025) 1385–1407, https://doi.org/10.1007/ s10845-023-02308-9.
- [125] Z. Wang, M. Li, F. Ren, B. Ma, H. Yang, Y. Zhu, Sobol sensitivity analysis and multi-objective optimization of manifold microchannel heat sink considering entropy generation minimization, Int. J. Heat Mass Transf. 208 (2023) 124046, https://doi.org/10.1016/j.ijheatmasstransfer.2023.124046.
- [126] Z. Guo, Q. Xu, M. Ni, A numerical study on the battery thermal management system with mini-channel cold plate considering battery aging effect, Appl. Therm. Eng. 219 (2023) 119564, https://doi.org/10.1016/j. applthermaleng.2022.119564.
- [127] W. Zhao, C. Meng, Y. Zhao, S. Xie, X. Wang, C. Jiang, W. Li, R. Jing, Research on aging-thermal characteristics coupling and aging thermal management analysis of large-capacity LiFePO4 battery, J Energy Storage 114 (2025) 115675, https://doi. org/10.1016/j.est.2025.115675.